An Integrated Design Study for an Advanced Tokamak to Close Physics Gaps in Energy Confinement and Power Exhaust

D. B. Weisberg,◯* J. Leuer, J. McClenaghan,◯ J. H. Yu, W. Wehner, K. McLaughlin, T. Abrams, J. Barr,◯ B. Grierson,◯ B. Lyons, J. R. MacDonald, O. Meneghini,◯ C. C. Petty, R. I. Pinsker,◯ G. Sinclair, W. M. Solomon,◯ T. Taylor, K. Thackston, D. Thomas,◯ B. van Compernolle, M. VanZeeland, and K. Zeller

General Atomics, PO Box 85608, San Diego, California 92186-5608

Abstract — *A high-level design study for a new experimental tokamak shows that advances in fusion science and engineering can be leveraged to narrow the gaps in energy confinement and exhaust power handling that remain between present devices and a future fusion pilot plant (FPP). This potential new U.S. facility, an Exhaust and Confinement Integration Tokamak Experiment (EXCITE), will access an operational space close to the projected FPP performance regime via a compact, high-field, high-power-density approach that utilizes advanced tokamak scenarios and high-temperature superconductor magnets. Full-device optimization via system code calculations, physics-based core-edge modeling, plasma control simulations, and finite element structural and thermal analysis has converged on a $B_T = 6$ T, $I_P = 5$ MA, $R_0 = 1.5$ m, $A = 3$, D-D tokamak with strong plasma shaping, long-legged divertors, and 50 MW of auxiliary power. Such a device will match several absolute FPP parameters: plasma pressure, exhaust heat flux, and toroidal magnetic field. It will also narrow or close the gap in key dimensionless parameters: toroidal beta, bootstrap fraction, collisionality, and edge neutral opacity. Integrated neutron shielding preserves personnel access by limiting nuclear activation and maximizes experimental run time by reducing site radiation. In addition to design study results and optimization details, parameter sensitivities and uncertainties are also discussed.*

Keywords — *Fusion pilot plant, integrated design, high-field tokamak, EXCITE, integrated tokamak exhaust and performance.*

Note — *Some figures may be in color only in the electronic version.*

I. INTRODUCTION

The Fusion Energy Sciences Advisory Committee,[1] in its 2020 long-range plan, has called for the design and construction of a new experimental fusion device to close the remaining "integrated tokamak exhaust and performance (ITEP)" gaps between present-day facilities and a future fusion pilot plant (FPP). This new tokamak facility, called the Exhaust and Confinement Integration Tokamak Experiment (EXCITE), is a carryover of a main recommendation of the 2020 U.S. Fusion Community Planning Process,[2] namely, the recommendation for a new tokamak user facility. These strategic reports specifically highlight the need for an experimental tokamak that meets two core criteria:

1. "The flexibility to investigate innovative tokamak divertor solutions, encompassing long-legged concepts and PFC material options, at heat and particle fluxes that are at the same scale as those projected for the pilot plant."

2. "The ability to simultaneously achieve these divertor solutions at core plasma energy confinement and bootstrap current fractions that project to a high-average-power output, net-electric pilot plant."

These experimental goals do not uniquely define the EXCITE design; indeed, the EXCITE parameter space is dependent on the target FPP design. It is therefore necessary to specify the FPP parameters first, and then design EXCITE to address the physics and technology gaps that arise on the path to that specific FPP.

Based on the recommendations from the previously noted reports, as well as the recent National Academies of Sciences, Engineering, and Medicine (NASEM) 2021 report,[3] this study will focus on the advanced tokamak (AT) approach to a compact, steady-state, net-electric FPP. In an AT, active control techniques are used to manipulate and optimize the plasma to obtain conditions scalable to robust operating points and high fusion gain for future fusion reactors. AT scenarios seek to achieve levels of fusion power similar to the conventional scenario but at lower plasma current for steady-state operation, and have been the focus of extensive study on both existing and planned tokamaks.[4–8] Such an approach has been considered in a number of previous studies, with varying levels of modeling fidelity and systems integration.[9–11] As will be discussed in this paper, the AT strategy is the logical choice for a high bootstrap current, high-pressure density plasma core that achieves net energy gain due to low recirculating power needs for auxiliary current drive (CD). This approach is complemented by the use of high-temperature superconducting (HTS) magnets[12,13] that permit a high toroidal field (TF) in a compact (moderate aspect ratio) device.

In addressing the task of designing a FPP, it is apparent that there is a natural tension between the dual needs for whole-device optimization and high-fidelity modeling. The need for optimization is driven by concerns that a fusion power plant must satisfy many criteria to be a successful endeavor, that is, not only must it generate net electrical power in a self-sufficient manner, but it also has to be economically, politically, and socially tenable. An iterative optimization study can minimize important factors like capital cost, levelized cost of electricity, startup tritium inventory, and site boundary radiation dose. However, the high-fidelity modeling tools that can best simulate these complex systems are not well suited for iterative optimization because they often require significant computing resources and operator scrutiny to verify the outputs. While these high-fidelity models can rigorously simulate a specific well-defined system, they are slow to map out the larger parameter space that is essential for optimization and comparison studies. This is a significant challenge that has yet to be overcome, and the results presented here entail one step toward a fully integrated solution.

The conceptual design for an EXCITE device is presented here as the result of a two-stage integrated optimization study. First, the General Atomics (GA) systems code[14,15] (GASC) is used to optimize the zero-dimensional (0-D) parameters for both a target FPP design space as well as the EXCITE facility that would close the relevant gaps toward that target. Second, the details of this EXCITE design point are verified using a suite of dedicated physics and engineering modeling tools, resulting in a three-dimensional (3-D) conceptual design of the whole-device build. This workflow relies on being both integrated and iterative. The reduced models in the systems code aim to resolve all conflicts between the many facility subsystems, while the detailed modeling that follows is meant to both verify the design point and identify any discrepancies in the systems code formalism. The two stages are iterated as needed until the final conceptual system design satisfies all of the initial constraints and goals. Since a strong emphasis is placed on integration between facility subsystems, the risk of subsystem incompatibility is minimized and the study output should be ready for detailed engineering design work.

This paper is organized as follows. The guiding physics missions and objectives for both the FPP and EXCITE targets are enumerated in Sec. II. The systems code optimizations of both facilities are presented in Sec. III. Then the high-fidelity modeling results for each of the major EXCITE subsystems are shown in the following sections: core plasma physics (Sec. IV.A), magnet design (Sec. IV.B), vertical stability and control (Sec. IV.C), exhaust power handling (Sec. IV.D), and nuclear shielding (Sec. IV.E). A glossary listing EXCITE parameter names and definitions is provided in the Appendix.

II. PHYSICS MISSION AND OBJECTIVES

The physics goals of both the FPP and EXCITE facilities have been derived from recommendations in the three U.S. fusion community reports highlighted previously. An overarching goal is that the FPP be a relatively low-capital-cost facility that demonstrates fusion power via the generation of net electricity in a self-sufficient manner. In this study, facility size is used as a proxy for capital cost and is therefore the main parameter in the FPP optimization function. The four main goals for the FPP considered here are

1. compact (low capital cost)

2. high plasma pressure (high fusion power density)

3. steady-state operation (high bootstrap fraction)

4. net electric [200 MW(electric)].

The specific choice of a 200-MW(electric) pilot plant was derived from the upper bound recommended in the NASEM report, which is in turn is based on the forecast of a growing role for intermediate-sized power generation stations in the U.S. energy grid. This also matches the power output in the CAT-DEMO study, which was an initial study to explore the design of a compact 200-MW(electric) facility. While previous concepts like the AIRES (Ref. 16) and DEMO (Ref. 17) studies focused on the lower levelized cost of electricity that is enabled by gigawatt-scale facilities, the CAT-DEMO results showed the feasibility of a compact FPP as a first-of-a-kind (FOAK) demonstration facility.

The CAT-DEMO results also detail the high leveraging effects of the AT approach, which utilizes both high plasma pressure, high bootstrap fraction, and fully noninductive CD. This advanced plasma core takes advantage of the high level of stability and control demonstrated in present-day tokamaks to achieve high fusion power with low parasitic expenditure on plasma CD. It will be shown that achieving simultaneously high levels of these two parameters, $<P>$ and f_{BS}, is a key goal on the path toward a compact steady-state FPP.

In addition to these key core plasma parameters, it is also critical to develop a solution for the high level of exhaust power that is endemic to the tokamak concept. A FPP that operates with a steady-state, noninductive core must be able to direct and dissipate the exhaust heat flux via a thermally equilibrated divertor region.[18,19] The main metric of this challenge is the heat flux into the divertor region, thus the FPP must be optimized for efficient fusion power generation so as to not require a prohibitive level of heating power. The AT approach is well suited to address this constraint, as the high bootstrap fraction reduces the auxiliary power required to sustain the plasma current and the high energy confinement reduces the fusion power required to sustain the core pressure. A core scenario with high confinement and a high bootstrap fraction will thus reduce power flowing into the divertor region, and thus permit a more compact device.

To close the gaps in these key core and exhaust parameters, the list of EXCITE experimental goals considered here are as follows:

1. Integrate a high-confinement AT plasma core with a dissipative, diverted plasma edge.

2. Simultaneously attain plasma pressure, bootstrap fraction, and exhaust heat flux that approach FPP-relevant conditions.

3. Maximize experimental utility by maintaining personnel access and high-duty-cycle operation.

4. Minimize capital cost and the design/construction timeline.

Finally, it is desirable that EXCITE also play a role in advancing fusion technologies to a readiness level appropriate for inclusion in a FPP design. The risk levels associated with FPP design, construction, and operation must be minimized either by standalone technology demonstrations or integration with the EXCITE mission. This includes innovation in superconducting magnets, plasma-facing components (PFCs), heating and current drive (H&CD) actuators, and plasma control systems. This study will show that the inclusion of some of these technologies enhances EXCITE capabilities, furthering the fusion relevance of its experimental mission. There are also a number of FPP-relevant technologies that cannot be demonstrated as part of the EXCITE program; nuclear-specific systems, including tritium fuel processing, tritium breeding blanket modules, and power conversion, are better suited for research and development independent of a tokamak device.

III. FACILITY OPTIMIZATION

The first stage of this design study, a systems-level optimization of the FPP and EXCITE concepts, was executed using GASC. GASC is a Python-based code that includes reduced models for all the major subsystems in a tokamak FPP: the plasma core, first wall and divertor, breeding blanket, nuclear shielding, magnet coils, H&CD actuators, fueling and fuel cycle, and balance of plant. Most tokamak subsystems are modeled in GASC in terms of 0-D parameters, while select components (e.g., core fusion reactivity and coil mechanical stresses) require one-dimensional (1-D) solutions to accurately capture the relevant physics and engineering processes. GASC also utilizes a sequential least-squares programming optimizer routine[20] that minimizes a target function while enforcing constraints on selected parameters.

The workflow for calculating an optimized solution for either a FPP or EXCITE consists of specifying an objective (cost) function, defining which input parameters are free to vary during the optimization search, and defining which input and output parameters are constrained. Free parameters are chosen to reflect the high dimensionality of potential operational spaces; common choices include fundamental plasma parameters, such as B_T, I_P, T_{i0}, and R_0, and as well as engineering parameters, such as the inboard radial build and structural composition of the central solenoid (CS) and TF coils. Constrained parameters are used to impose limits on key subsystems. Core plasma performance is primarily bounded by stability limits (β_N, safety factor, Greenwald fraction) and performance targets (bootstrap fraction, energy confinement factor scaling), while

engineering constraints are applied to magnets (structural stress, conductor current density), PFCs (peak neutron power load, divertor heat flux), and H&CD actuators [power fraction (L-H) power threshold, electron cyclotron (EC) access]. These details for the FPP and EXCITE design studies are presented in Table I.

The objective function defines the goal of the optimization and is the primary distinction between the FPP and EXCITE models presented here. As stated earlier, the FPP goals are to generate 200 MW(electric) of net power in a compact device; here, compact is interpreted as having a small major radius. Thus, the FPP objective function is simply the device major radius, which acts to minimize the size of the facility given a fixed net power output

$$F_{\mathrm{FPP}} = R_0 \ . \tag{1}$$

The sensitivity of the optimized solution to a particular constraint can be evaluated by scanning over a range of constraint values. In the case of FPP optimization, it is informative to model how the solution changes with respect to the bootstrap fraction and allowed divertor heat flux. Figure 1 shows the results of this FPP optimization scan, with the maximum constraints on f_{BS} varied from 0.2 to 0.9 and $P_{\mathrm{SOL}}B_\theta/R$ varied from 15 to 50 MW T/m. This sensitivity study maps out a region in f_{BS} to $<P>$ space, and shows that a 200-MW(electric) FPP can be as compact as $R_0 = 4.5$ m. The device size is minimized by increasing the allowable divertor heat flux and/or bootstrap fraction; however, the most extreme cases for both of these scanned parameters are disallowed due to other constraints. The $f_{BS} \leq 0.9$ solutions result in lower f_{BS} due to the onset of the pedestal density constraint $f_{\mathrm{GW},ped} \leq 0.9$. Similarly, the highest divertor heat flux solutions at $f_{BS} = 0.9$ are less than the maximum allowed value of 50 due to the onset of the EC access constraint $\omega_{pe0}/\omega_{ce0} \leq 1$, where ω_{pe0} is the plasma electron frequency and ω_{ce0} is the EC frequency, both evaluated at the equilibrium magnetic axis. Notably, these additional constraints are not limiting for the majority of the FPP design points.

The condition of core $T_i/T_e \sim 1$ is an optimum condition for a D-T fusion reactor because while high ion temperature is desired for high fusion power, the majority

TABLE I

Optimization Settings for GASC Modeling*

Constrained Parameters		Free Parameters	Constant Parameters	
Coil peak stress	≤ 800 MPa	(Major radius)	T_{e0}/T_{i0}	1.0
Coil J_{crit}/J	≥ 2.0	(Aspect ratio)	δ	0.8
f_{BS}	$\leq 0.8^{\mathrm{a}}$	TF	f_κ	0.95
$f_{\mathrm{GW,ped}}$	≤ 0.9	Plasma current	Shield thickness	$0.1(R_0 - a)$
$\beta_N/\beta_{N,IW}$	≤ 0.8	Ion temperature	Vacuum vessel/ blanket thickness	0.2/1.0 m
f_{L-H}	≥ 1.0	CS coil radial build	Ion species	D-D/D-T
$q^\star$	≥ 3.0	TF coil radial build	η_{aux}	0.4
H_{DS03}	≤ 1.0	CS coil structural fraction	$\eta_{thermal}$	0.4
EC core access $(\omega_{pe0}/\omega_{ce0})$	≤ 1.0	TF coil structural fraction	$\eta_{reclaim}$	0.6
Poloidal heat flux $(P_{\mathrm{SOL}}B_\theta/R)$	$\leq 35.0^{\mathrm{a}}$ MW T/m		$M_{blanket}$	1.25×
N_{wall}	≤ 2.0 MW/m²		f_{BoP}	0.07
Net electric power	$-/200$ MW(electric)		H&CD actuator	EC

*Where two values are given, they apply to the EXCITE/FPP studies, respectively. Free parameters in parentheses were held constant for EXCITE modeling.
aA constraint that was scanned over a range of values; the given value is what was chosen for the FPP target design point.
TF = toroidal field.

⊗ANS
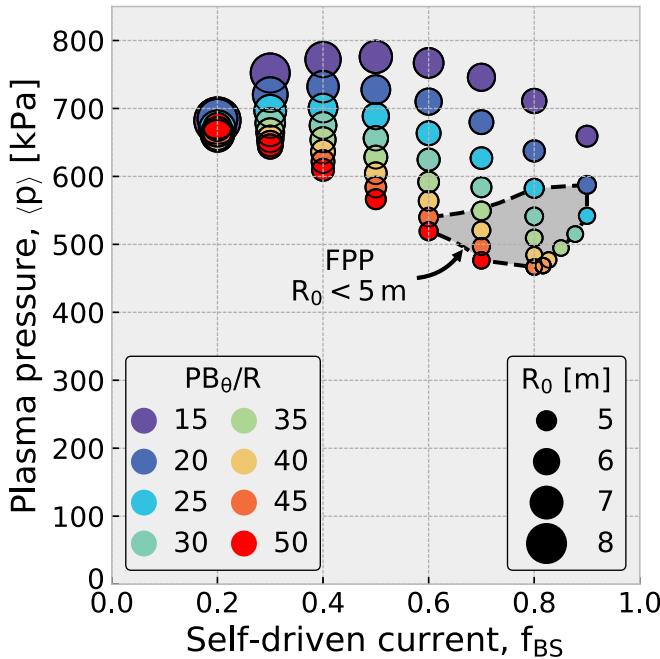
Fig. 1. FPP optimization sensitivity scan in bootstrap fraction and divertor heat flux. The highlighted area shows the most compact 200-MW(electric) solutions (major radius less than 5 m). Certain extreme combinations of bootstrap fraction and heat flux are disallowed by other constraints, namely, the Greenwald density limit and core EC access requirement.

of the heating power will be passed instead into the electrons (via alpha heating). It is possible that a high core density will be sufficient to thermally equilibrate the ions and electrons, but in the absence of this, some amount of auxiliary ion heating will be needed. Thus, the exclusive use of EC heating is not a strict requirement for the FPP (or EXCITE). Instead, the criterion of EC as the primary H&CD actuator, as listed in Table I, serves as a worst-case set of constraints on the FPP optimization. First, it limits the core density, such that EC access is possible. Second, it determines the efficiency using the electron cyclotron current drive (ECCD), which is one of the least-efficient CD actuators. Because the core access and CD efficiency will be higher for other types of H&CD actuators, this ensures a conservative optimization point and allows for substitution of other types of H&CD in the event that $T_i/T_e \ll 1$. An example of this is seen in Sec. IV.A where the STEP modeling results for the EXCITE noninductive case include 10 MW of core ion cyclotron (IC) heating in order to raise T_i/T_e, as well as to increase on-axis current density.

It is important to note several critical differences between the results presented here and in other fusion power plant design studies. While the GASC code can accurately recreate systems code solutions for the ARC (Ref. 9), ARIES (Ref. 10), and FNSF (Ref. 21) reactor designs, those facilities were designed using a different combination of engineering and physics constraints. For example, the FNSF and ARC designs take advantage of a bucked support scheme between the TF and CS coils that alleviates stress in both components. This can allow for a higher toroidal magnetic field, which in turn can result in a more compact device (ARC: $B_T = 9.2$ T and $R_0 = 3.3$ m; FNSF: $B_T = 7.5$ T and $R_0 = 4.8$ m). However, this advanced engineering technique is currently at a low technology readiness level and imposes additional constraints on CS coil segmentation, and so is not used in the results presented here. Similarly, the choice of electrical output also has a large impact on the final baseline design. The ARIES reactor study, which targets a 1-GW(electric) net electric facility to be representative of a FOAK commercial power plant, predicts fusion gain $Q_{plasma} > 25$ for each of its four candidate designs. A FPP like the one considered here, however, needs only achieve 200 MW(electric) to allow for extrapolation to a FOAK commercial plant. Since efficient electricity generation is not a primary goal for a FPP, this manifests in a lower $Q_{plasma} = 12.6$.

The FPP design point chosen to guide EXCITE optimization is presented in Table II. This 0-D solution is close to the global minimum in major radius and was selected so that the required bootstrap fraction and divertor heat flux were realistically achievable in a nuclear reactor. Figure 2 shows that the FPP size plateaus for $P_{SOL}B_\theta/R > 35.0$ MW T/m and $f_{BS} > 0.8$, as other constraints become limiting factors. In fact, there is only a 5% decrease in R_0 from the starred FPP solution to the minimum R_0 solution. The chosen threshold value of $P_{SOL}B_\theta/R = 35$ for the divertor heat flux metric is comparable to several other proposed compact, high-field facilities: 31 for SPARC, 33 for ARC, and 35–58 for the ARIES-ACT designs. This fully noninductive FPP solution generates 847 MW of fusion power and 200 MW(electric) of net electric power, with an optimized aspect ratio of slightly above 3 and a high poloidal beta core.

An important constraint is the energy confinement time, which is calculated based on a H-mode scaling relation

$$H_{DS03} = 0.028 I_P^{0.83} B_T^{0.07} n_{e,19}^{0.49} P_{SOL}^{-0.55} R_0^{2.11} A^{-0.3} \kappa^{0.75} M^{0.14} \,,$$

$$(2)$$

where H_{DS03} is a gyro-Bohm-like confinement scaling first published in Ref. 22. Though it was motivated by the observed beta-independence of thermal energy confinement on the DIII-D, it is derived via a power-law least-squares fit

TABLE II

Systems Code Optimized Design Points for FPP and EXCITE*

Parameter	Unit	FPP	EXCITE			
			Inductive A	Inductive B	Noninductive A	Noninductive B
R_0	(m)	4.55	1.50			
a	(m)	1.39	0.50			
B_T	(T)	6.0	6.0			
$B_{max,TF}$	(T)	16.8	14.3			
κ		2.3	2.3			
δ		0.8	0.8			
P_{aux}	(MW)	67	50			
I_P	(MA)	9.5	4.74	4.89	2.51	3.43
β_N		3.11	2.16	2.99	2.42	3.19
β_T	(%)	3.6	3.4	4.9	2.0	3.6
β_P		2.16	1.10	1.47	2.33	2.24
f_{NI}		1.0	0.51	0.69	1.0	1.0
f_{BS}		0.8	0.43	0.57	0.9	0.87
$<P>$	(kPa)	510	488	698	289	522
$q^\star$		7.8	6.4	6.2	12.1	8.8
f_{GW}		0.84	0.49	0.47	0.92	0.67
$<T>$	(keV)	11.6	5.0	7.2	3.0	5.4
$<n>$	(10^{20}m^{-3})	1.33	2.93	2.93	2.93	2.93
T_0	(keV)	26.1	11.3	16.2	6.7	12.1
n_0	(10^{20}m^{-3})	1.58	3.49	3.49	3.49	3.49
$v_e^\star$	($\times 10^{-2}$)	2.51	6.49	3.15	33.84	7.90
$\rho^\star$	($\times 10^{-3}$)	2.95	5.40	6.46	4.16	5.59
$P_{SOL}B_\theta/R$	(MW T/m)	35.0	33.8	34.4	18.1	24.4
H_{DS03}		1.0	1.0	1.4	1.0	1.4
H_{98y2}		1.44	1.13	1.57	1.21	1.63
P_{fusion}	(MW)	847	(31.4)	(75.1)	(9.0)	(66.1)
P_{net}	(MW)	200.0	–	–	–	–
Q_{plasma}		12.6	(0.69)	(2.08)	(0.18)	(1.46)
Q_{engr}		1.76	–	–	–	–
N_{wall}	(MW/m^2)	2.0	(0.62)	(1.49)	(0.18)	(1.31)

*Four possible EXCITE scenarios are considered: inductive and fully noninductive CD, each with nominal and enhanced energy confinement factor (H_{DS03} = 1.0, 1.4). EXCITE values in parentheses indicate the expected results for D-T operation.

to the edge-localized modes (ELM) H-mode database (DB3.5) used for the ITER project. Thus, it should be comparable to the $H_{98Y,2}$ scaling in terms of cross-device applicability. The use of H_{DS03} is motivated in this study due to its scaling versus plasma beta, which matches experimental findings in high-beta AT experiments.[23] The ITER H-mode energy confinement factor $H_{98Y,2}$ scaling,[24] on the other hand, has been observed to underpredict thermal energy confinement at high beta,[25] and thus would result in overly pessimistic predictions of energy confinement in a high-beta tokamak. The baseline optimization constrains this scaling relation to 1.0, which corresponds to H_{98y2} = 1.44; this is within reasonable expectations for an AT core scenario at high β_P (Refs. 26 through 29).

The EXCITE facility has a different set of motivating considerations. Namely, it should find a balance between (1) achieving FPP-relevant parameters and (2) keeping cost and construction time to a minimum in order to meet community targets of subsequent FPP operation in the 2040s. In this study, an a priori device size was chosen for the EXCITE design, with the understanding that a DIII-D (Ref. 30), ASDEX-U (Ref. 31), KSTAR (Refs. 32 and 33), or EAST (Ref. 34) size tokamak is more feasible to design and construct in a 5- to 10-year period than a larger facility. Furthermore, the EXCITE aspect ratio should be chosen to approximate the expected FPP design, such that experimental results do not need excessive scaling in that parameter. Thus, the

⊗ANS
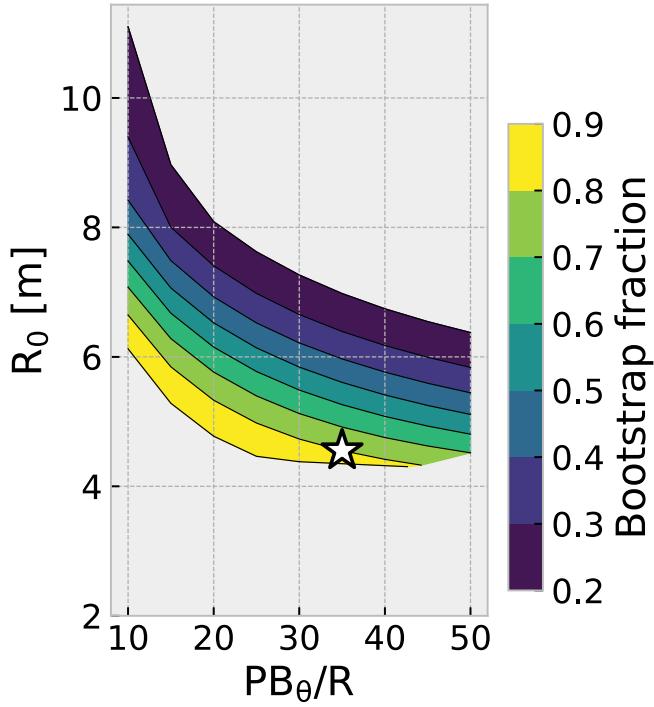
Fig. 2. FPP optimization sensitivity scan from Fig. 1 presented as a function of poloidal divertor heat flux. The objective function R_0 is shown on the y-axis, with contours indicating the bootstrap fraction constraint. The white star shows the selected FPP design point described in Table II and is close to the minimum size while allowing for slight margins below the most extreme bootstrap fraction and heat flux.

EXCITE objective function reduces to the maximization of the plasma pressure given a fixed major radius $R_0 = 1.5$ m and aspect ratio $A = 3$:

$$F_{\mathrm{EXCITE}} = - <P> . \qquad (3)$$

Within this optimization framework, the EXCITE device has another degree of freedom that the FPP does not: inductive versus noninductive operation. As an experimental facility, EXCITE will be able to run either with inductive CD (allowing maximum plasma pressure and current) or with fully noninductive CD (where absolute plasma pressure is traded for a higher bootstrap fraction and more advanced core). This is most effectively controlled in systems code modeling by imposing the noninductive fraction as a limiting constraint (instead of the bootstrap fraction). In determining the best EXCITE design, the question is whether to optimize the maximum plasma pressure for an inductive or noninductive core; here we chose the first option, which serves to maximize the absolute plasma performance relative to the auxiliary power. This is seen in Fig. 3 where the optimized solutions for both cases are

shown as a function of B_T. The noninductive optimization leads to lower I_P and much higher P_{aux} compared to the inductive optimization, with only slight differences in the peak pressure and TF. Choosing the inductive optimization results in a more efficient device at a lower safety factor and power, which can also explore fully noninductive scenarios at a lower plasma current and pressure. It is notable that the resulting solutions still optimize to a moderate $q_{95} \approx 6$, which is far from the kink stability limit and in a regime with measurably reduced disruption risk.[29]

Based on the FPP design target heat flux metric ($P_{\mathrm{SOL}} B_\theta / R = 35$), the EXCITE baseline inductive design optimizes to $B_T = 6$ T with a maximum $I_P = 5$ MA and $P_{aux} = 50$ MW (Fig. 3). The maximum TF is determined in this regime by both the coil stress limits and the divertor heat flux limits, which combine to locate the maximum plasma pressure at a q_{95} that is well above the kink stability threshold. Given this fixed TF strength, a scan of optimized EXCITE solutions is shown in Fig. 4, where each point corresponds to a specific pair of noninductive fraction and divertor heat flux constraints. Higher plasma pressure is possible with higher heat flux limits, with the caveat that the required H&CD power also increases. While the highest heat flux limits allow the EXCITE solutions to overlap the FPP parameter space, these points require auxiliary heating in excess of 75 MW. If the total auxiliary power is limited to 50 MW, then there is still a gap between the EXCITE and FPP parameter spaces. Still, the maximum EXCITE performance with this additional constraint narrows the total gap from present-day facilities by more than half. A full list of parameters for these two specific cases are enumerated in Table II with $H_{DS03} = 1.0$, alongside the corresponding solutions for an enhanced confinement scenario at a higher energy confinement scaling factor $H_{DS03} = 1.4$.

The preceding integrated systems code optimization has produced target 0-D designs for both the FPP and EXCITE concepts, and it is worth commenting on some of the resulting features. Due in part to the shared constraints (especially the divertor heat flux), both devices have the same TF, $B_T = 6$ T, and comparable levels of auxiliary power. This is important for the development of FPP CD actuators. In the case of ECCD, the systems tested and operated on the EXCITE facility will be directly transferable to the succeeding FPP facility. The gyrotron frequency required for these cases is approximately 170 GHz, similar to the requirement under development for the ITER ECCD systems.[35]

Finally, it is interesting to calculate the potential for this EXCITE design point to conduct D-T experiments. Table II shows (in parentheses) the D-T performance for each EXCITE scenario. Notably, the enhanced confinement cases would exceed fusion break-even and could
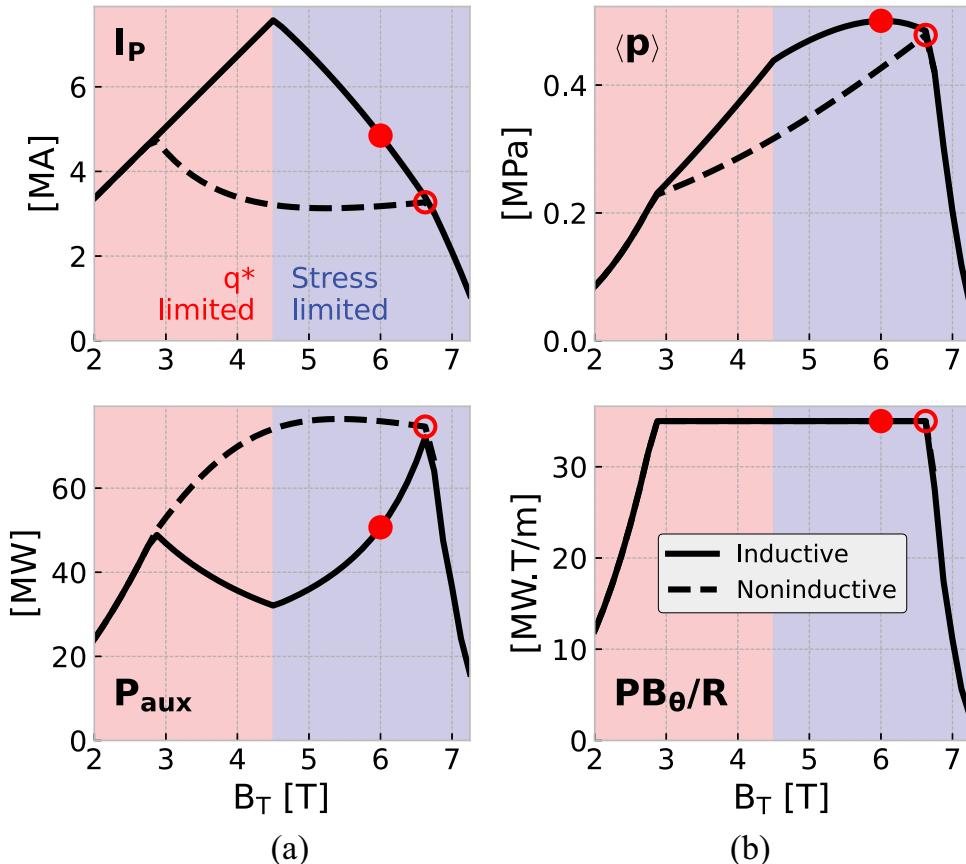
Fig. 3. Optimization of the toroidal magnetic field for two $R_0 = 1.5$ m and $A = 3$ EXCITE scenarios: inductive (solid) and noninductive (dashed). The shaded regions correspond to where the inductive case is limited by (a) the edge safety factor constraint and (b) the coil stress constraint. Circles indicate the maximum pressure for the inductive (filled) and noninductive (open) scenarios.

even achieve $Q \approx 2$ under optimistic projections. While this D-T capability is not part of the EXCITE mission, it is nevertheless a good indicator of the high core performance that will close the remaining gaps in preparation for the first AT FPP.

IV. HIGH-FIDELITY MODELING

Having completed the systems code optimization of both the FPP and EXCITE concepts, the next step is to verify the EXCITE solutions with high-fidelity physics and engineering computational models. These models include dedicated plasma physics simulation tools (STEP core modeling,[36] SOLPS-ITER exhaust modeling,[37] TokSys control modeling[38,39]), as well as physics/engineering codes (COMSOL Multiphysics, OpenMC neutronics simulation).[40] While some models are limited to two-dimensional (2-D) axisymmetric representations of the tokamak, the construction of a full-device 3-D EXCITE build is necessary to integrate all of the separate models discussed in the following sections.

Figures 5, 6 , and 7 show the full-device EXCITE design, with major subsystems labeled. Several key design elements have been incorporated in anticipation of the primary experimental goals of the facility. The vacuum vessel is designed as a 20-cm-thick, double-walled, stainless steel vessel with an average 10-cm-thick interstitial layer of water for cooling and radiation shielding. This dual functionality allows the device to be run at a high power density without overheating the internal components or damaging the magnet coil conductors via high neutron flux. Additional neutron shielding layers in front of the TF coils further reduce nuclear activation of materials outside the vacuum vessel.

The poloidal layout of the EXCITE cross section is designed to integrate the confinement and exhaust experimental missions. The plasma core is strongly shaped, with high elongation and triangularity to leverage predicted gains in normalized stability and confinement, as well as expected access to advanced operation via the high beta poloidal,[26] high q-min,[41] or super H-mode[42] scenarios. The plasma is nominally high elongation, double-null geometry with extended vertical space for long-legged divertors and

⊗ANS
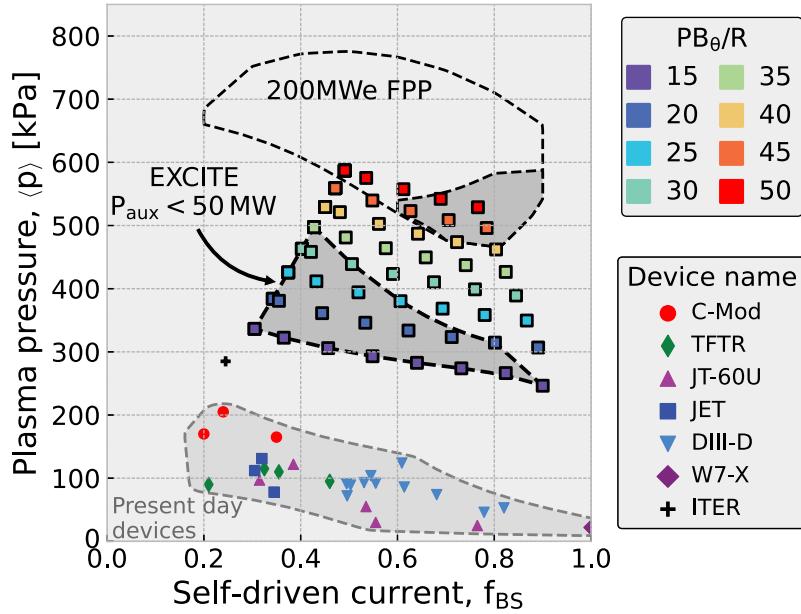
Fig. 4. Sensitivity scan of the $R_0 = 1.5$ m, $A = 3$, $B_T = 6$ T, and $H_{DS03} = 1.0$ EXCITE design showing scans in noninductive current fraction and divertor heat flux. The 200-MW(electric) FPP target space from Fig. 1 is shown (dashed outline), as well as the subset of this space where $R_0 < 5$ m (shaded). Additionally, the subset of the EXCITE optimization space where auxiliary power is limited to below 50 MW is highlighted. Present-day experimental results and the projected $Q = 10$ ITER scenario (cross) are below for comparison.[42,69,74–82]

Fig. 5. Three-dimensional computer-aided design renderings of the baseline EXCITE design point showing all major subsystems, including superconducting CS and TF coils, copper divertor and vertical stability coils, double-walled vacuum vessel, cryostat, gravity supports, and auxiliary infrastructure. While the neutral beam H&CD is not explicitly considered in this study, this design does allow for the possibility of multiple beam lines.

dedicated copper coils for vertical stabilization, strike-point control, and experimental flexibility.

IV.A. Core Plasma Physics

The EXCITE core performance parameterized by GASC was verified by core integrated modeling using the OMFIT STEP module. STEP is an integrated core modeling framework that combines an arbitrary number of standalone codes into one cohesive suite of simulation tools; commonly used codes include EFIT (Ref. 43) or CHEASE (Ref. 44) for plasma equilibrium, EPED (Ref. 45) for pedestal stability, NEO (Ref. 46) for bootstrap current, ONETWO (Ref. 47) for ohmic current diffusion, TGYRO (Ref. 48) for transport calculations with TGLF and NEO transport models, and the OMFIT CHEF module for H&CD sources. Global stability is checked using the ideal magnetohydrodynamic (MHD)
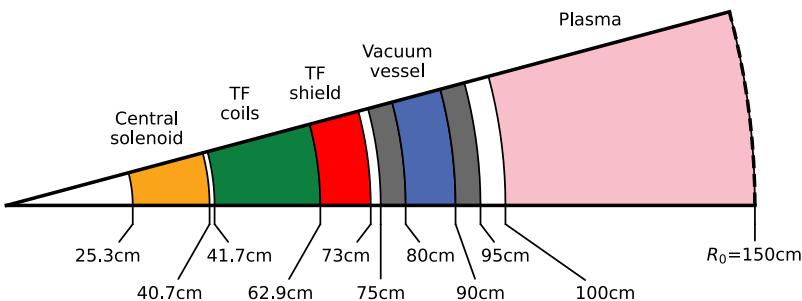
Fig. 6. One-dimensional inboard radial build for the baseline EXCITE design point. All spaces are vacuum gaps, except for the water-filled interstitial gap between the vacuum vessel walls.
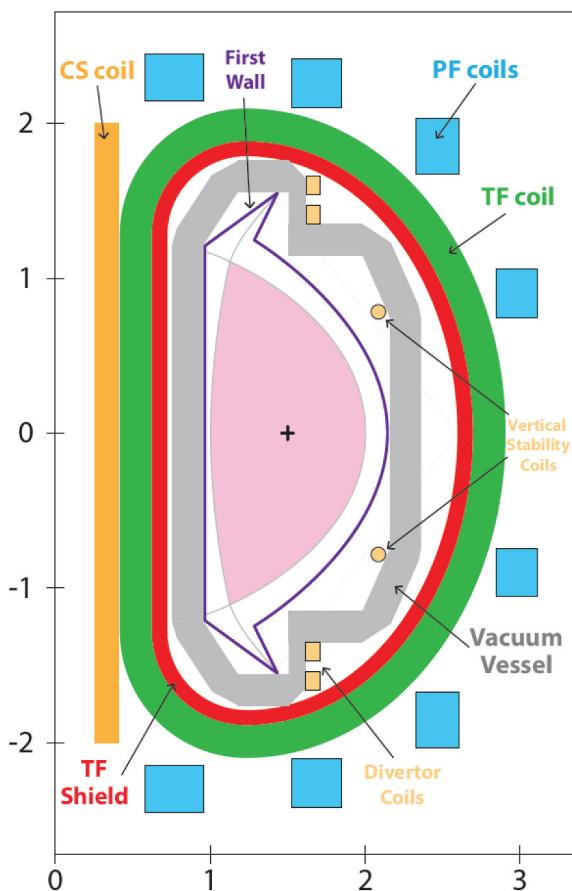
Fig. 7. Two-dimensional poloidal build for the baseline EXCITE design point. Dimensions are in meters.

code DCON (Ref. 49). EPED pedestal modeling assumes a standard ELMy H-mode edge transport barrier, while TGLF core transport modeling allows for the possibility of an internal transport barrier (ITB) as well. A user-defined cycle of these codes is iteratively run until convergence, producing a self-consistent integrated model of the tokamak core.

Two EXCITE core scenarios are modeled using STEP: a high-current inductive scenario and a low-current noninductive scenario. The GASC optimization

results (Table II) are used as a starting point for plasma shape, current, and kinetic profile initialization. The H&CD is limited to electron and IC wave injection, and the total auxiliary power is limited to 50 MW. The converged STEP parameters are listed in Table III, and the 1-D plasma profiles are shown in Fig. 8. In generating these integrated solutions, the most important variables were found to be the electron cyclotron heating and ECCD aiming specifications; the exact locations of H&CD have a large impact on the global energy confinement and bootstrap current. For a given set of global parameters, there is only a small set of viable EC aiming trajectories that produce the desired current density profile and energy confinement time. The existence of these EC-compatible solutions is therefore an additional constraint that is not reflected in the GASC optimization study.

The inductive solution, with its less stringent requirement for noninductive CD, is achieved with 100% EC heating and minimal auxiliary CD. This case utilizes the maximum $I_P = 5$ MA, of which 38% is bootstrap current. The high core EC heating results in a large $T_{e0}/T_{i0} = 1.9$, but the corresponding H_{98y2} confinement factor is still 25% higher than the nominal ITER H-mode database scaling. The core density is limited by the EC cutoff constraint, with the on-axis electron density just slightly higher than the cutoff threshold; all EC power is deposited around $\rho \sim 0.23$. The volume-averaged plasma pressure is 519 kPa, comparable to the target FPP design space and higher than any present-day tokamak.

The noninductive solution, requiring a more specialized current density profile to achieve fully noninductive operation, has a mix of EC and IC heating with significant off-axis EC deposition. The high β_P produces a large Shafranov shift, making core EC deposition a challenge at a fixed gyrotron frequency. Thus, 10 MW of IC injection is required to both heat the core and drive the core current to avoid the potentially unstable effects of strong negative

⊗ANS

TABLE III

Integrated Modeling Results from OMFIT STEP for an
Inductive and a Noninductive EXCITE Scenario

Parameter (Unit)	EXCITE Inductive	EXCITE Noninductive
B_T (T)	6.0	6.0
I_P (MA)	5.00	3.36
q_{95}	5.80	9.35
P_{aux} (MW)	50 (EC)	34 (EC), 10 (IC)
$<P>$ (kPa)	519	437
$li(3)$	0.60	0.41
f_{BS}	0.38	0.68
f_{NI}	0.40	1.0
f_{GW}	0.42	0.64
β_N	2.18	2.99
β_P	1.03	2.30
H_{DS03}	1.13	1.15
H_{98y2}	1.25	1.31

magnetic shear near the magnetic axis. The 34 MW of EC is used to drive off-axis current, producing a strong pressure gradient at mid-radius and enhancing the bootstrap fraction to 68%. This large off-axis deposition of heating power also reduces the energy confinement because the effective minor radius is reduced to a fraction of the nominal distance,

resulting in an energy confinement factor of only $H_{98y2} = 1.31$ despite the large Shafranov shift. This noninductive solution is not fully optimized in terms of the CD profile, and there are likely significant improvements that can be made with further refinement of the ECCD aiming and alignment with the mid-radius ITB. However, even with significant potential for additional optimization of the current profile, this solution achieves a volume-averaged plasma pressure of 437 kPA, which is close to the target FPP parameter space at a comparable bootstrap fraction.

Both scenarios generally match the EXCITE parameter space predicted by GASC (Fig. 9), exceeding the baseline $H_{DS03} = 1.0$ solutions and individually (but not simultaneously) matching the target FPP bootstrap fraction or pressure. Compared to the corresponding GASC solutions, the modeled bootstrap current fraction is lower than expected, while the pressure is higher. This can be partially attributed to the lower β_P achieved in the STEP solutions and partially to the uncertainty in the value of the empirically derived bootstrap coefficient employed in GASC in this parameter regime. The large deposition of heating power at mid-radius reduces the heating efficiency and decreases the poloidal beta relative to what would be expected
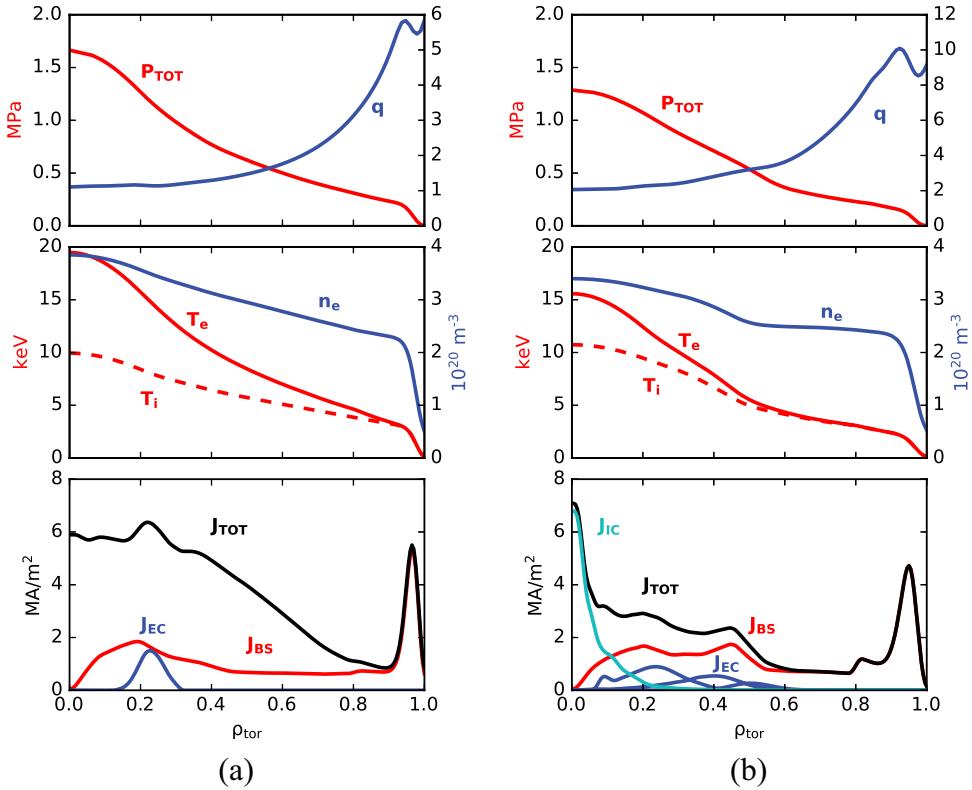
Fig. 8. Core plasma STEP solutions for EXCITE (a) $I_P = 5.0$ MA inductive and (b) $I_P = 3.36$ MA noninductive scenarios.

with a similar current density profile with core-localized heating. This highlights a major experimental challenge of noninductive EXCITE operation: developing an FPP-relevant scenario without core alpha heating from fusion reactions. To produce a high-pressure, high bootstrap fraction AT core, a FPP should be able to achieve good energy confinement while simultaneously optimizing the current profile; however, EXICTE will need to judiciously divide its available auxiliary power between core heating and off-axis CD. Furthermore, the EXCITE solutions presented previously are very close to the EC density cutoff threshold, making current profile optimization a challenge; the corresponding FPP solutions have ample headroom in the core density limit and do not suffer this same complication. While these STEP results indicate high performance in both EXCITE scenarios, more modeling and experimental research are needed to optimize the current profile for FPP-relevant operation.

While the impact of intrinsic impurities was not considered in the integrated core modeling, it is important to comment on the possible repercussions of trace levels of low- and high-Z species. First-wall materials, while not specified in this preconceptual design study, can have a large impact on the transport, stability, and overall performance of the plasma core. A primary goal of EXCITE will be to close this part of the core-edge integration gap by identifying a plasma-facing material that can withstand the high heat flux, minimize erosion and re-deposition, and

coexist with a high-performance core at acceptable concentrations; demonstrating low tritium retention is equally important, although outside of the stated EXCITE mission. Possible material candidates include tungsten, beryllium, and silicon carbide, all of which would have a range of differing impacts that are difficult to fully capture with the modeling tools used in this study. The down-selection of a first-wall material is thus left to a later stage in the EXCITE design process.

IV.B. Magnet Design

The systems code optimization of the CS and TF magnets was verified using an integrated COMSOL finite element model of the entire coil and plasma geometry. The 2-D axisymmetric poloidal field (PF) and segmented 3-D TF model simultaneously integrate the magnetic fields from the 16 distinct TF coils, six distinct CS coils, eight poloidal shaping coils, and the toroidal plasma current. The TF coil shape follows an approximately constant-tension Princeton-D geometry,[50] with the center post legs supported in a wedged configuration. The TF and CS coils are freestanding in that there is no bucking action between the two magnet systems. The shaping coil currents are optimized to create the target plasma shape, as well as to produce the necessary flux null geometry for inductive plasma breakdown and current ramp up. The EXCITE TF coil outboard legs are located at the proper distance from the plasma to result in a TF ripple amplitude of 0.5% at the midplane outboard plasma boundary.

The radial build and current density for the EXCITE magnet systems was taken from the GASC results, and the resulting structural stresses on the coils were calculated in the COMSOL finite element analysis model. Two specific states in a typical plasma discharge were considered: the initial magnetization (IM) state of the PF system just prior to plasma breakdown and the end of the PF flux–driven plasma current ramp when noninductive systems are expected to generate substantial CD. These cases represent the two extremes for CS coil current, and thus the two extremes of CS coil stresses. The major system code parameters $B_T = 6$ T and $I_P = 5$ MA were inputs to the various finite element modules. The IM PF current states were determined to ensure good plasma breakdown with the absolute magnitude of flux set to center the IM and final plasma state to produce equal stresses in the CS. This optimization established the IM state flux at 6 Vs, and the resulting PF current states were used in the finite element model to establish the CS stress state.

The Von Mises stresses calculated in the CS coil for both states are shown in Fig. 10; the GASC constraint of
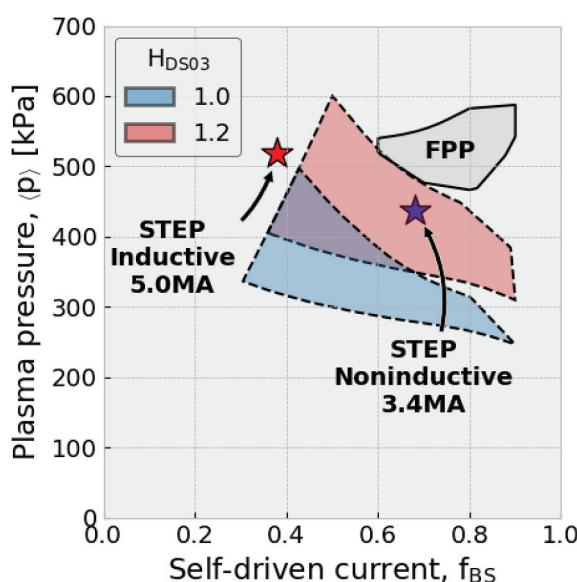
Fig. 9. Comparison of STEP inductive and noninductive scenarios to GASC-optimized solutions for fixed-energy confinement scaling factors of $H_{DS03} = 1.0$ and 1.2.

800 MPa is almost exactly duplicated in the quasi 3-D finite element analysis. The TF coil Von Mises stress distribution is shown in Fig. 11a, where again the peak stress is the GASC constraint value of 800 MPa. For these global simulations, each coil is represented as a homogeneous component with the relative structural properties of stainless steel modified to compensate for the fraction of nonstructural material, i.e., superconductor, stabilizing substructure, and insulation and coolant voids. The structural fraction of the structure is 47% for the CS coils and 64% for the TF coils. The nonstructural part contains a 10% void (coolant and insulator) and the
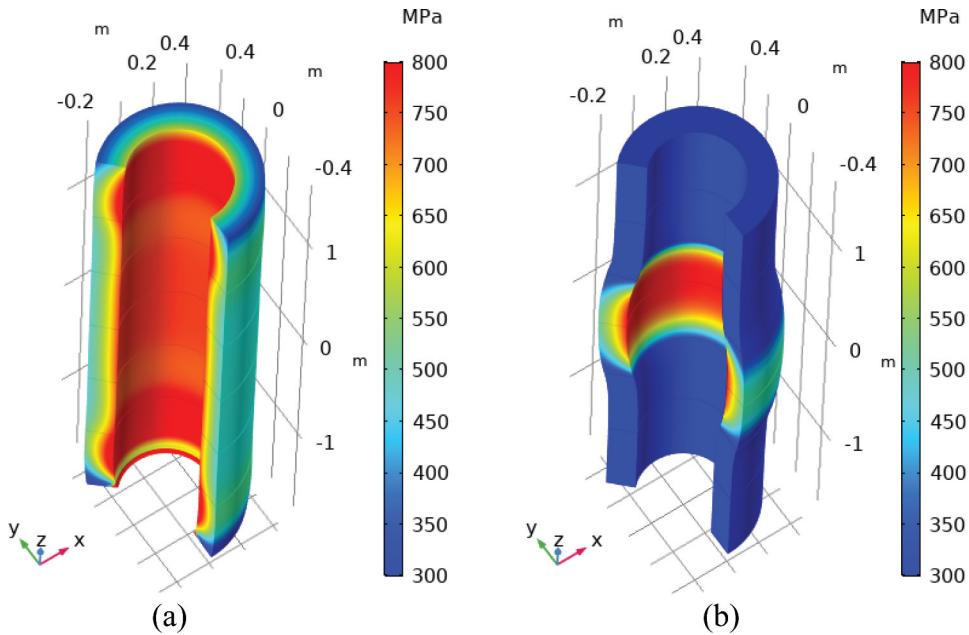
Fig. 10. Finite element stress analysis of two specific states of the center solenoid: (a) IM at 6 Vs and (b) end of the flux-driven plasma current ramp. The freestanding coil is modeled as a homogeneous stainless steel structure with the modulus of elasticity scaled to match the volumetric ratio of load-bearing material. The peak Von Mises stresses calculated in each case do not exceed the 800-MPa limit.
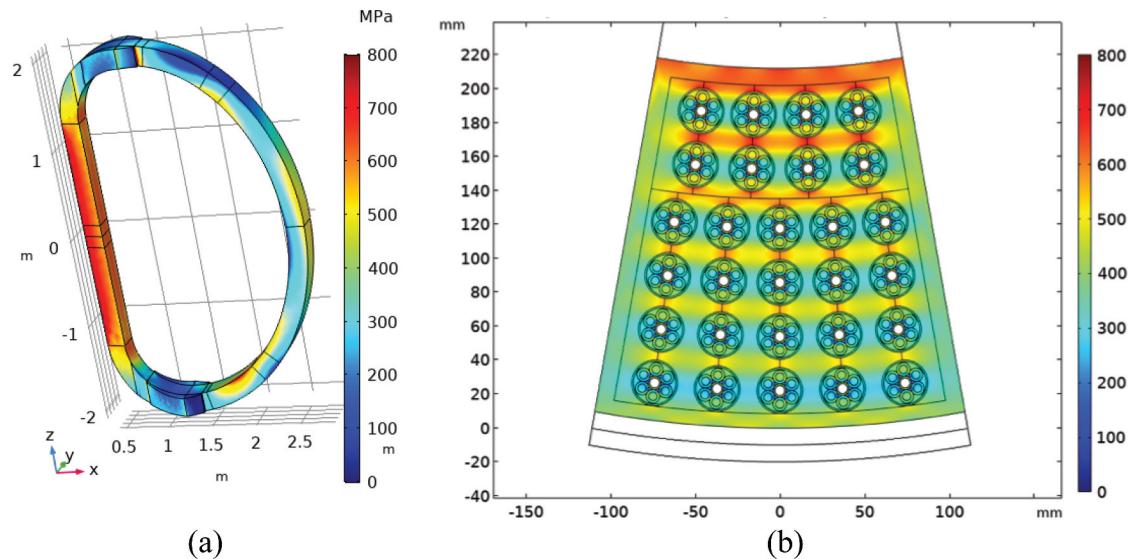
Fig. 11. Finite element stress analysis of a single TF coil at maximum field ($B_T = 6$ T). (a) The wedged coil is modeled as a homogeneous stainless steel structure with the modulus of elasticity scaled to match the volumetric ratio of load-bearing material. (b) The winding pack layout is modeled at the inboard midplane with detailed CICC-CORC conductors arranged in a wedged pattern with stainless steel radial plates. The peak Von Mises stresses calculated in each case do not exceed the 800-MPa limit.

HTS superconductor has 50% HTS ribbon and 50% Cu stabilizer. Note that this model assumes that the conductor material is not load bearing. The TF coil legs are augmented by a stainless steel case with antitorque interconnects that are approximately simulated in the finite element model. This casing and antitorque structure is necessary to reduce out-of-plane forces to below the stress limit and includes cutouts for port placement and attachment points for gravity supports.

A conceptual design for the center post TF coil conductor pack is modeled in a 2-D COMSOL finite element simulation utilizing the CORC cable-in-conduit conductor (CICC) configuration currently under development by Advanced Conductors, Inc. (Refs. 51 and 52). This HTS cable is being designed specifically for magnetic fusion energy applications and is estimated to have the capacity of up to 100 kA per conductor. A novel 28-turn, arch-supported winding layout is proposed for this TF coil design where radial steel plates act as wedges between azimuthally displaced conductors, each of which contains six parallel CORC cables and a central cooling channel. Instead of using a large "nose" support structure to withstand all of the radial force, these radial wedge plates distribute the majority of the centering force throughout the structure. Finite element modeling shows an even distribution of stress at the center post midplane, which maintains the peak Von Mises stress below 800 MPa (Fig. 11b). This TF coil winding pack design also satisfies the magnet quench handling requirement, which sets a lower bound on the volume of copper available to transiently dissipate the quenched current without exceeding the conductor failure temperature.

Finally, the flux coupling between the plasma and the CS coil is modeled to ensure that the projected CS current swing is sufficient to drive the required plasma current to flattop. A nominal DIII-D discharge is scaled to the EXCITE plasma geometry, and the inductive coupling between the plasma and the poloidal coils is modeled throughout the ramp-up period. The calculated Ejima coefficient is constant and very close to the GASC estimation (Fig. 12), confirming that the optimized coil radial build is sufficient to drive up to 5 MA.

IV.C. Vertical Stability and Control

Critical to an AT high plasma performance in a compact device like EXCITE is the ability to attain high plasma elongation, with values approaching the highest value achieved in standard aspect ratio tokamaks like the DIII-D. Critical to high elongation is robust stabilization of the resulting highly unstable vertical motion. To this end, the systems code approximation of the plasma vertical stability was verified using the
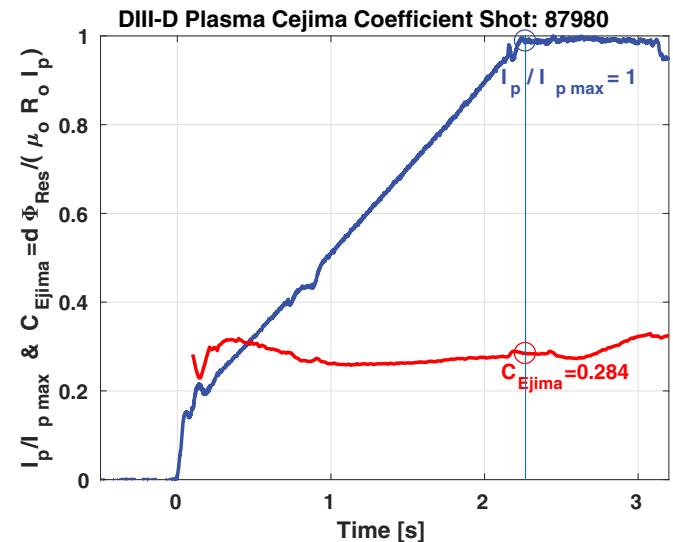
Fig. 12. Modeled flux coupling between plasma and poloidal coils during nominal EXCITE current ramp to maximum $I_P = 5$ MA. Equilibrium evolution is scaled based on DIII-D shot 87980. The calculated Ejima coefficient[83] is constant and very close to the GASC estimation.

TokSys tokamak control modeling suite.[38,39] While the GASC uses an empirical equation for the maximum stable elongation as the primary constraint for plasma shape, TokSys is a robust and mature code suite that self-consistently models the coupled electromagnetic system comprised of the plasma and surrounding active and passive conducting domains. TokSys was used here to evaluate the capability of the EXCITE shaping coils and in-vessel coils to control vertical excursions and to determine whether passive stabilization plates are required.

The TokSys model of the EXCITE electromagnetic coupled system is shown in Fig. 13a. The double-walled vacuum vessel and superconducting CS coils (not shown) are modeled, and a set of copper coils inside the TF bore are included for divertor geometry shaping and vertical stability control. The TokSys equilibria are solutions to the Grad-Shafranov equation with simple parametrized radial profiles, and the global plasma parameters are self-consistently fitted to match the EXCITE inductive solution in Table III. The divertor coils allow for flexible control of outer strike point positioning and are necessary to produce the desired long-legged divertor geometries (Fig. 13b).

The extent to which the vertical instability of this strongly shaped equilibrium can be controlled is analyzed by calculating the largest rigid-body vertical displacement dz_{max} that can be successfully stabilized by the in-vessel vertical control coils (assuming conventional power supplies).[53] Typically, a well-controlled plasma has

$dz_{max} \geq 0.1a$, with a being the minor radius; here, this corresponds to $dz_{max} \geq 5$ cm. Figure 14 shows the results of this analysis, where dz_{max} is calculated as a function of the plasma inductance. Systems with and without passive stabilizing plates are considered, and both cases show adequate vertical control for $li(3) \leq 0.73$. Both the inductive and noninductive STEP solutions have plasma inductance within this stable regime. It is particularly notable that passive stability plates may not be necessary for vertical control; the thick vacuum vessel itself provides a considerable level of passive stability alongside the in-vessel vertical stability coils. Higher inductance equilibria (typical of L-mode discharges) will not be able to achieve similar elongations to the target scenarios discussed earlier, but it is conceivable that evolution to higher elongation can be attained after H-mode transition.

The magnetic geometry considered in this study is an up-down symmetric double null, with two X-points and presumed equal power sharing between the upper and lower divertors. However, it is important to note that such an equilibrium is notoriously difficult to control, both from a magnetic and heat flux perspective.[54] It will probably be more feasible to operate in a slightly biased double-null configuration ($dR_{sep} < 1\%$ of minor radius) where a primary X-point serves as the main location of power exhaust, while still allowing the high plasma elongation made possible by the double-null flux distribution. A key part of the experimental mission of EXCITE would be to develop the correct control algorithms to robustly access this magnetic geometry, as well as to investigate the role of edge drifts in dividing the exhaust heat flux between two nearly balanced divertors.

IV.D. Exhaust Power Handling

The predicted EXCITE divertor power and particle fluxes were modeled using the SOLPS-ITER code,[37] which couples the 2-D fluid plasma transport code B2.5 (Ref. 55) and the 3-D kinetic neutral transport code EIRENE (Ref. 56). Deuterium plasmas were simulated using tungsten walls and divertors with the EIRENE particle reflection model. Sputtered tungsten impurities were not included in the model since tungsten

(a)   (b)
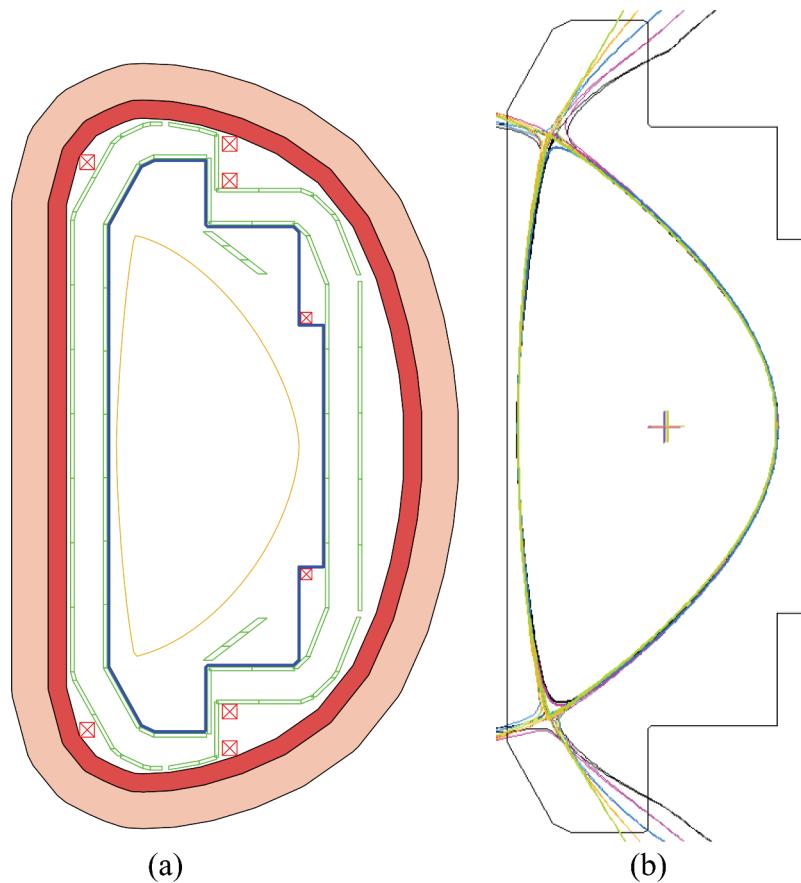
Fig. 13. TokSys model of the EXCITE (a) electromagnetic coupled system, including copper divertor (ex-vessel) and vertical stability (in-vessel) coils and passive plates, and (b) the flexible control of both divertor strike point locations.
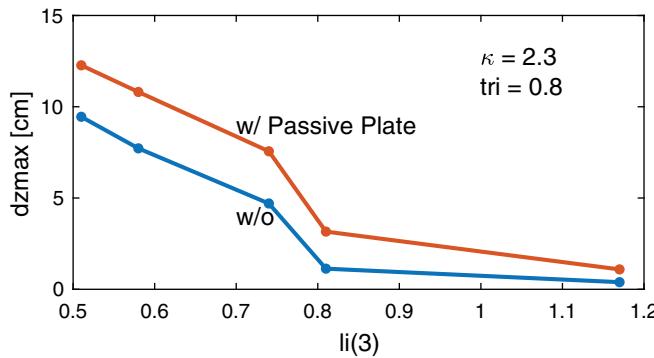
Fig. 14. Vertical stability analysis of the EXCITE system over a range of plasma self-inductances. Acceptable control corresponds to $dz_{max} < 5$ cm, which is achieved at low $li(3)$ both with and without passive stability plates.

has a relatively low sputtering yield by deuterium, and because tungsten ionization and radiation do not contribute significantly to the volumetric power balance in the divertor and scrape-off layer (SOL). Three computational grids corresponding to different divertor geometries were constructed using the same double-null equilibrium magnetic geometry, which is calculated by the TokSys modeling suite. All grids have a spatial resolution of 120×36 cells in the poloidal and radial directions, respectively. At the inner boundary of the grid, the plasma power flux was split evenly between electrons and ions, and the power flux at the low-field side of the grid inner boundary was set to $3\times$ that at the high-field side to approximate the effect of ballooning transport. The quoted powers are the input powers to the simulation that represent the heating power minus core radiated power for steady-state conditions. The cross-field transport coefficients were set spatially constant, with particle diffusivity $D = 0.3$ m^2/s and electron and ion thermal diffusivities $\chi_e = \chi_i = 1.0$ m^2/s.

Viscosity particle drifts were included in the model, but $E \times B$ and $B \times B$ drifts were not included. While drifts have indeed been shown to significantly affect divertor conditions both in experiments and modeling, numerical instabilities (most likely arising from highly sheared grid cells) prevent most high-power drift cases from converging. For the drift cases that have converged in the slot-flat case, it has been observed that the up-down power imbalance does not significantly differ from the no-drift cases, provided that the slot remains detached while the lower flat divertor remains attached. Fundamentally, it appears that asymmetry between the upper and lower divertor plasma conditions drives the up-down power imbalance, and those asymmetries can be caused by divertor shapes, $E \times B$ flows, and/or pumping asymmetry.

A variety of divertor baffle strategies were considered in a double-null configuration, and the resulting heat flux and target temperatures were compared. Figures 15a, 15b, and 15c show the three permutations of flat (open) and slot (closed) baffle geometries for the upper and lower outer divertors, respectively, flat-flat, slot-flat, and slot-slot. The modeled outer strike point target temperatures in the upper and lower divertors are plotted versus separatrix density in Figs. 15d and 15e for injected power levels of 20 and 50 MW. It can be seen that divertor geometry has a strong effect on the onset of detachment, which is indicated by the condition $T_{e,target} < 10$ eV. As shown in previous numerical studies[57,58] and experiments,[59,60] closed divertors require a lower upstream density for detachment due to neutral trapping and increased power dissipation.

A number of additional observations on divertor performance can be made from Fig. 15 and include (1) higher power plasmas require higher density for detachment, as expected; (2) upper and lower divertors behave the same when the divertors are up-down symmetric in simulations without magnetic drifts; and (3) in the slot-flat divertor configuration, there is a drastic asymmetry in divertor performance, with the slot divertor electron temperature at the outer strike point being much colder than in the flat divertor. Further analysis reveals that power flow in the outer SOL of double-null simulations is strongly affected by the up-down symmetry of the divertor geometries, with power preferentially flowing toward the open divertor. However, note that up-down power sharing asymmetry is expected to also be affected by particle drifts, which are not included here.

The poloidal and surface heat flux at the lower divertor target is shown in Fig. 16 for 50 MW of input power at three different edge densities for the slot-slot divertor configuration. The surface heat flux at $n_{e,sep} = 1.1 \times 10^{20}$ m^3 was found to have a peak value of approximately 40 MW/m^2, which is above the tungsten damage threshold of 15 MW/m^2 (Ref. 61). At a similar upstream density of $n_{e,sep} = 1.2 \times 10^{20}$ m^{-3} in the flat-flat divertor configuration, the peak surface heat flux was 130 MW/m^2. The reduced heat flux in the slot-slot configuration is due to the trapped neutral deuterium concentration in the closed divertor geometry, as well as the shallower angle between the flux tube and target surface.

As a comparison to these results, a 0-D power balance based on 50 MW crossing the separatrix and a λ_q of 0.31 mm as predicted by Eich's scaling of the SOL power fall-off length (regression 14 in Ref. 18) yields an unmitigated parallel heat flux of $q_{\parallel} = 11.6$ GW/m^2. A factor
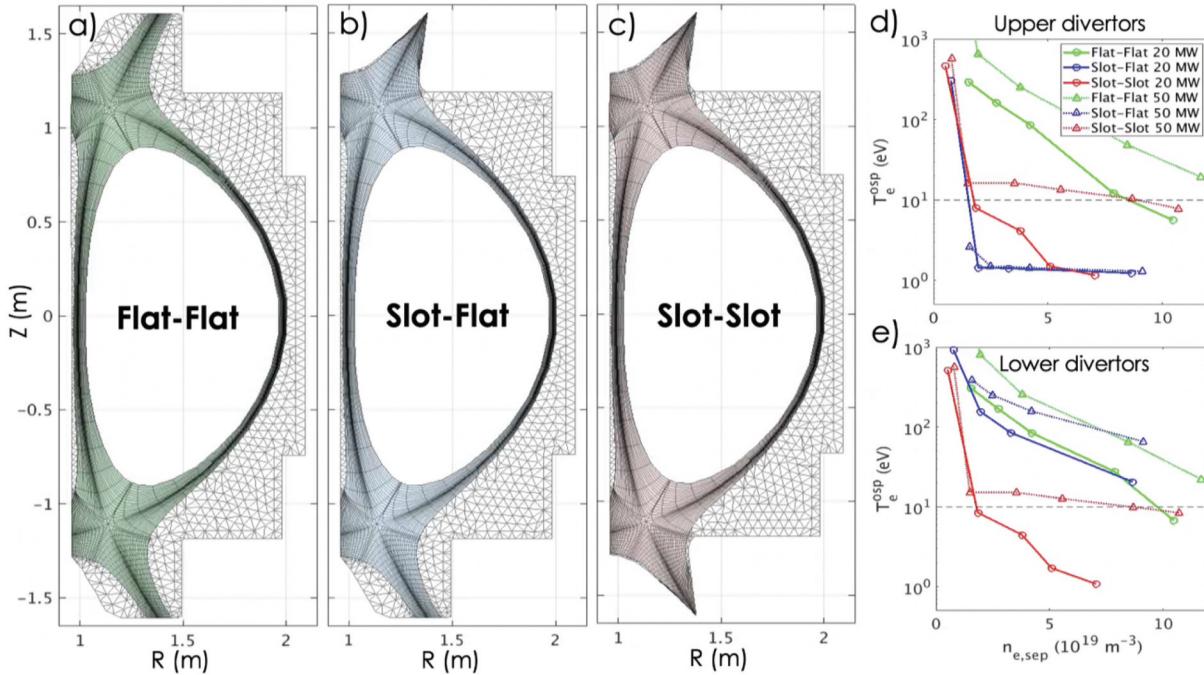
Fig. 15. SOLPS-ITER modeling of three different divertor baffle strategies: (a) symmetric flat (open), (b) asymmetric flat (open) and slot (closed), and (c) symmetric slot (closed). The target temperatures for two different input power levels (20 and 50 MW) are shown for each case in (d) and (e) as a function of midplane separatrix electron density. The nominal detachment threshold of 10 eV is shown, and is achieved by the slot-slot geometry.
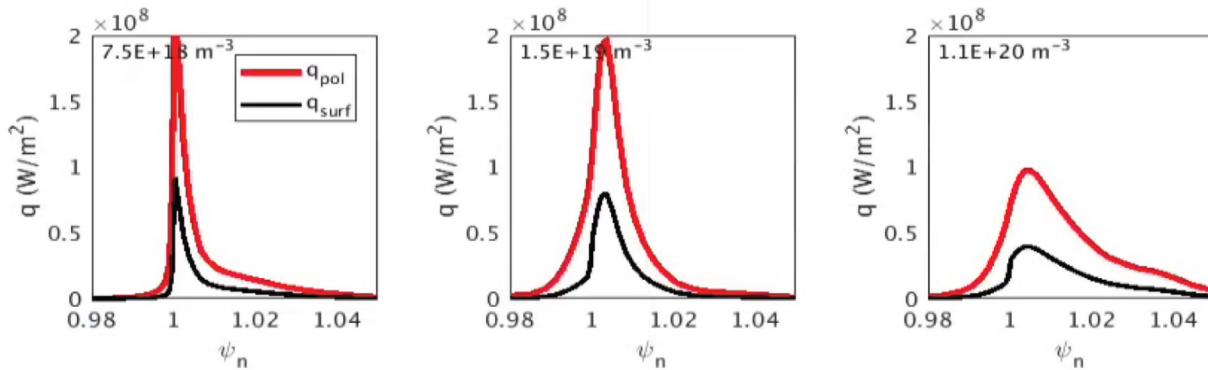
Fig. 16. Poloidal and surface heat flux profiles at the lower divertor target in the 50-MW slot-slot configuration for three different separatrix electron density levels. Without impurity radiation, the highest density case has a peak target heat flux of 40 MW/m^2.

of 1/2 optimistically assumes equal power sharing between the upper and lower outer divertors. A flat target surface that is orthogonal to flux surfaces would be subject to an unmitigated heat flux of $q_{pol} = q_{surf} = 1190$ MW/m^2; for a divertor target plate tilted with an angle between the target normal and flux surfaces of 75 deg, the unmitigated deposited heat flux to each target surface would be $q_{surf} = 310$ MW/m^2, which is still well above material limits. The primary reason for this significant difference from the SOLPS-

ITER simulations is the heat flux width, where a larger $\lambda_q = 1.1$ mm was calculated. These two results illustrate both the uncertainty in divertor modeling as well as the potential range in radiative dissipation required to reduce the deposited heat flux below the material limit of 15 MW/m^2.

This 0-D estimate indicates that the required power dissipation in the EXCITE SOL/divertors could be as high as 95% compared to the SOLPS-ITER prediction of only 62.5%. Both cases would provide an excellent test bed for

heat exhaust solutions such as impurity seeding, which will further enhance power dissipation beyond what has been shown here. Seeded impurities can provide access to divertor detachment,[62,63] but the impurities must be controlled in order to prevent degradation to core plasma performance. Recent experiments with nitrogen and neon seeding in the small angle slot divertor at the DIII-D have demonstrated promising results in which full detachment was observed while maintaining high core confinement.[64] This challenge of core-edge integration in reactor-relevant regimes is one of the main missions of the EXCITE facility, and therefore additional modeling should be conducted with impurity seeding to predict if the divertor surface heat flux can be reduced below the tungsten damage threshold, as well as to predict the effect of impurities on pedestal pressure and core performance.

While transient power loads like ELMs were not included in the divertor heat flux modeling, it is apparent that such phenomena would impart excessive heating to the EXCITE PFCs. Thus, EXCITE would need to be operated in an ELM-free or ELM-mitigated mode, either using active control (via 3-D ELM suppression coils) or using a core scenario that has naturally small/grassy ELMs (e.g., the high beta poloidal or steady-state hybrid scenarios). These small ELM scenarios are particularly synergistic with the noninductive AT path envisioned in this study. Demonstrating this goal of achieving acceptable transient-edge power loads while maintaining the high core confinement typical of AT scenarios is a prime example of the critical core-edge integration gap that the EXCITE facility will seek to close on the path to a FPP.

IV.E. Nuclear Shielding

A 3-D neutronics model of the EXCITE tokamak was developed for analysis of shielding and dose rates. The geometries of the tokamak, machine pit, and building were constructed using Paramak[65] and converted to Direct Accelerated Geometry Monte Carlo (DAGMC) models[66] using Cubit.[67] The DAGMC models were then used as the geometry inputs for coupled neutron-photon Monte Carlo transport simulations in OpenMC (Ref. 40).

The neutronics model of the tokamak includes EXCITE's channeled vacuum vessel design, first wall, TF coils and their respective shields, PF coils, the CS, copper shaping coils, port cutouts, and a simplified cryostat. The machine pit and building construction simulated in the model are primarily based on the building and shielding construction of the DIII-D National Fusion Facility. The model of the machine pit includes a concrete wall, a wall extension made of borated polyethylene on top of the concrete wall, and a roof made of a layer of 1% borated gel surrounded by steel. The building walls and roof are modeled as a layer of steel. The site boundary in this study is defined as the cylinder with an inner radius of 100 m. The central plane of the tokamak is placed at ground level, and the floor of the machine pit and the ground are modeled as concrete. The configuration of the machine pit and building structure in this model holds similarities to previous neutronics models of the DIII-D (Ref. 68).

To measure the effects of the shielding components of the EXCITE tokamak, simulations were run with and without the shielding features of the device and the dose rates were compared. In the unshielded case, the first wall, the vacuum vessel channel, the outer vacuum vessel wall, the TF coil shields, and the cryostat were all removed from the model, leaving only the inner vacuum vessel wall as an approximation for the DIII-D vacuum vessel. The shielding components were then added back into the model and total shielding factors were calculated. Four different vacuum vessel fill materials were compared: air, stainless steel, water, and 3% borated water (Fig. 17).

Compared to the simulations without shielding features, the EXCITE tokamak's site boundary dose rates were significantly reduced. In particular, the models with water filling the vacuum vessel channel performed the best in terms of shielding factors: borated water and pure water yielded total shielding factors of 11.1 and 10.6, respectively. Given the predicted peak neutron rate of 10^{17} n/s, and comparing these reductions in site boundary dose to the current DIII-D peak performance discharges, it is reasonable to conclude that EXCITE operation limits would be similar to those imposed by the DIII-D discharges with 10^{16} n/s. Maximum performance scenarios on the DIII-D generate 2 to 3×10^{16} n/s, so these shielding choices for EXCITE would permit roughly the same level of experimental run time as occurs during present-day DIII-D operations.

V. SUMMARY

An integrated design study was conducted for a new experimental tokamak facility with the goal of closing the remaining scientific and technical gaps between present day devices and a future FPP. This new facility, EXCITE, has been identified by several recent strategic planning reports[1,2] as an optimal solution for the U.S. fusion program to close the ITEP gap. In this study, a two-stage workflow was followed to optimize the high-level tokamak design and then verify the detailed subsystem specifications. First, GASC was utilized to optimize the 0-D solutions for a target 200-MW(electric) compact
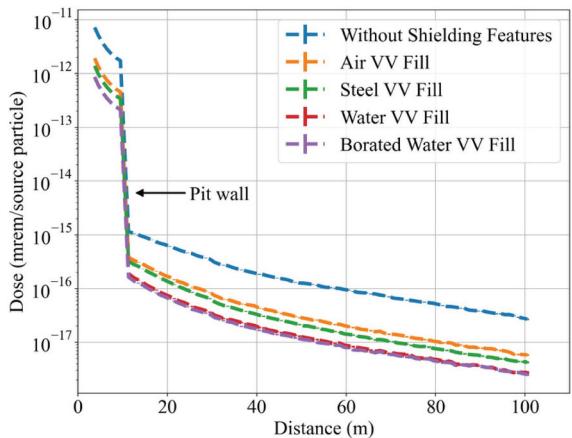
Fig. 17. OpenMC modeling of total (neutron and gamma) radiation dose per source neutron for five different EXCITE shielding strategies. The addition of the water-filled vacuum vessel to the DIII-D–like baseline case decreases the site boundary dose rate by approximately one order of magnitude.

FPP, with sensitivity scans in both bootstrap fraction and divertor heat flux. Then the same optimization procedure was used to optimize an EXCITE design that maximizes plasma pressure in a $R_0 = 1.5$ m and $A = 3$ device. Two specific inductive and noninductive solutions were chosen for high-fidelity verification via the STEP code, which confirmed the predicted core performance achieved with up to 50 MW of EC and IC auxiliary H&CD. The other major tokamak subsystems were also modeled to verify the systems code calculations: coil structural mechanics via finite element modeling, plasma shaping and vertical stability via TokSys, exhaust power handing via SOLPS-ITER, and radiation shielding via OpenMC. There is ample opportunity for improving the capability of the GASC, with transport and stability neural net modeling providing a fast way to more accurately calculate parameters such as bootstrap coefficient, pedestal height, and energy confinement time. Still, this whole-device EXCITE conceptual design is self-consistent and fully integrated, with all the high-level conflicts between the device requirements and subsystems resolved.

In conclusion, while all subsystem approximations by GASC were verified by the individual high-fidelity models, several critical challenges also were identified. First, the detailed core performance predictions by STEP-integrated modeling demonstrate the importance of energy confinement in the AT scenario. The choice to pursue a high bootstrap current fraction at a high poloidal beta necessarily forces the FPP and EXCITE optimizations to a regime of lower absolute performance. This is offset by the gains from higher energy confinement time that lead to

higher beta and plasma pressure. Demonstrating the successful extrapolation of these AT scenarios to a reactor-relevant regime should be a key mission of the fusion community and will be facilitated by EXCITE.

Second, the SOLPS-ITER simulations of divertor heat flux indicate that handling the power exhaust in a compact, high-field device will be the most challenging aspect of this approach to a FPP. High levels of impurity radiation will be required in a closed divertor region in order to dissipate up to 95% of incident heat flux and allow for reliable detachment. Furthermore, this local impurity concentration must be robustly controlled and prevented from impacting the core plasma confinement. An EXCITE facility as set out here would clearly help narrow science and technology gaps to a FPP; as recommended by the FESAC panel,[1] the fusion community must now move to establish the mission need for the facility and whether the investments required represent the best approach to close gaps for a FPP.

The international fusion community has recognized the importance of high magnetic fields in solving the ITEP gap between present-day tokamaks and future net-electric facilities, and there are a number of new high-field experimental tokamaks already under design and/or construction. It is informative to compare the designs of these devices to the EXCITE design presented here, and to highlight similarities and differences. Table IV lists the parameters of five high-field experimental tokamaks alongside the two EXCITE scenarios presented in Sec. IV.A. In terms of magnet technology, cryogenically cooled copper magnets were used by the C-MOD tokamak and will be used in the planned COMPASS-U, while the DTT and ITER tokamaks will use low-temperature superconducting magnets (Nb_3Sn and NbTi). On the other hand, both EXCITE and SPARC plan to use HTS magnets, which allow for higher conductor current density and coil field. As mentioned previously, SPARC plans to use a bucked coil support scheme that will allow for a record high B_T, but this engineering technique is currently at a low technological readiness level.

The main differentiation between EXCITE and these other devices is the target plasma scenario, as seen in the proposed plasma beta. The baseline operation strategy for all other tokamaks is low beta and inductive, using the well-established understanding of tokamak physics to produce a reliable but conservative operational scenario. The EXCITE mission instead pursues the goal of high energy confinement at high beta, utilizing AT scenarios developed over the past 10 years to produce high plasma pressure while simultaneously achieving a large bootstrap current fraction. These two different approaches can produce similar levels of exhaust heat flux, especially in compact devices like SPARC and EXCITE, though SPARC relies on augmenting its

TABLE IV

Comparison of High-Field Tokamak Operating Parameters*

Parameter (Units)	C-MOD	COMPASS-U	DTT	SPARC	ITER	EXCITE	
Scenario	EDA H-mode	Full Heating, High Current	Single-Null H-mode	Full-Field H-mode	Q = 10 Baseline	Inductive	Steady State
R_0 (m)	0.67	0.9	2.19	1.85	6.2	1.5	1.5
a (m)	0.22	0.27	0.7	0.57	2.0	0.5	0.5
A	3.0	3.3	3.1	3.2	3.1	3.0	3.0
κ	1.72	1.8	1.8	2.0	1.85	2.3	2.3
B_T (T)	5.7	5.0	6.0	12.2	5.3	6.0	6.0
I_P (MA)	1.4	2.0	5.5	8.7	15.0	5.0	3.4
P_{heat} (MW)	5.4	18	45	41	150	50	44
f_{GW}	0.54	0.32	0.42	0.37	0.85	0.42	0.64
f_{BS}	0.24	0.17	0.16	0.2	0.15	0.38	0.68
β_T (%)	1.6	2.7	2.2	1.3	2.5	3.6	3.3
β_N	1.4	1.8	1.7	1.1	1.8	2.2	3.0
β_P	0.6	0.5	0.4	0.5	0.7	1.0	2.3
q_{95}	3.6	2.5	2.6	3.1	3.1	5.8	9.4
P/R (MW/m)	8	16	15	16	24	31	27
PB_T/R (MW T/m)	46	80	90	191	128	186	163
PB_θ/R (MW T/m)	7	16	16	31	24	35	21

*Selected operating parameters for past [C-MOD (Ref. 69)] and future [COMPASS-U (Ref. 70), DTT (Ref. 71), SPARC (Ref. 72), and ITER (Ref. 73)] high-field experimental tokamaks listed for comparison alongside the inductive and steady-state EXCITE scenarios. The C-MOD reference scenario is an EDA H-mode at high field and current (discharge 1160930033), while the other device scenarios are the highest performance inductive operating points predicted in their respective publications.
EDA = enhanced D-alpha.

H&CD power with power from D-T fusion reactions in order to achieve its target operational regime. This AT approach also results in a high q_{95} edge safety factor in both EXCITE scenarios, which means that disruptions should be less damaging and occur with a lower likelihood when compared to the low q_{95} scenarios associated with conventional H-mode scenarios.[29]

The procedure described in this study was developed for use on a variety of tokamak design projects, ranging from experimental devices to FPP facilities. It is streamlined for repeated use, with the goal of providing a range of device designs that can be downselected based on subjective criteria. The selection of a FPP design is of particular interest in the near term, with the 2021 NASEM report calling for a finalized conceptual design by 2028. This workflow can be utilized to produce a variety of FPP designs that meet a set of predetermined requirements, with each design exploring a different set of trade-offs. For example, the technological readiness level (TRL) of FPP subsystem technologies is a key metric for design downselection. Limiting risk by allocating low-TRL solutions to different subsystems will produce very different FPP designs. The choice between

high temperature superconductor, bucked coil support, and high divertor heat flux can be explored using this workflow, and the integrated designs resulting from each approach can be compared and contrasted.

Future design studies for FPP facilities will need to consider a number of synergies between subsystem requirements beyond what has been presented in this study. The control requirements for a FPP are expected to be much more exacting than present-day devices due to the harsh nuclear environment and the thick breeding blanket that must be located between control diagnostics/actuators and the plasma. The specifications for the tritium fuel cycle are dependent on the performance of the burning core, which has parameters such as tritium burnup rate and impurity species that are expected to have an outsized impact on the tritium extraction, processing, and storage strategies. The blanket and divertor maintenance strategy will also have a strong impact on the global design, as the choice between horizontal and vertical ports or demountable device sectors will affect the TF coil requirements, plasma stability limits, and tritium breeding efficiencies. The trade-offs between these options will be explored in future upgrades to the integrated design workflow presented in this paper.

⊗ANS

APPENDIX

GLOSSARY

The following glossary contains a list of the parameters used in this design study, along with the corresponding definitions, symbols, and/or abbreviations.

TABLE A.I

Glossary of Parameter Names and Definitions

Symbol	Parameter Name	Definition
A	Aspect ratio	Ratio of plasma major radius to minor radius
a	Minor radius	Radial distance from plasma center to boundary at midplane
$B_{max,TF}$	Field at TF coil	Maximum magnetic field at TF coil conductor
B_T	Toroidal magnetic field	TF strength at plasma center
B_θ	Poloidal magnetic field	PF strength at outboard midplane plasma edge
C_{ejima}	Ejima coefficient	Quantification of flux coupling between CS coil and plasma
f_{BoP}	Balance-of-plant fraction	Power usage by non-H&CD systems, as a fraction of thermal cycle power
f_{BS}	Bootstrap fraction	Ratio of bootstrap current to total plasma current
f_{GW}	Greenwald fraction	Ratio of volume-averaged plasma density to Greenwald density limit
$f_{GW,ped}$	Pedestal Greenwald fraction	Ratio of pedestal density to Greenwald density limit
f_κ	Elongation fraction	Ratio of elongation to maximum stable elongation[84]
f_{L-H}	L-H power fraction	Ratio of P_{SOL} to threshold exhaust power for transition from L- to H-mode
f_{NI}	Noninductive fraction	Ratio of noninductively driven current to total plasma current.
$H\&CD$	H&CD	Hardware choice(s) for auxiliary heating and noninductive CD
H_{DS03}	Gyro-Bohm confinement factor	H-mode gyro-Bohm energy confinement scaling relation[22]
H_{98y2}	IPB confinement factor	H-mode ITER physics basis energy confinement scaling relation[24]
I_P	Plasma current	Total current inside plasma boundary
$li(3)$	Plasma inductance	Self-inductance of parallel plasma current profile
$M_{blanket}$	Blanket power multiplier	Power multiplier due to exothermic nuclear reactions in blanket
n_{e0}	Core electron density	Electron density at magnetic axis
N_{wall}	Neutron wall loading	Power incident at first wall due to primary fusion neutron flux
$<P>$	Plasma pressure	Total volume-averaged plasma pressure
Q_{plasma}	Fusion power gain	Ratio of P_{fusion} to P_{aux}
Q_{engr}	Engineering power gain	Ratio of gross electric power generation to parasitic power use
$q^\star$	Edge safety factor (zero dimensions)	Approximate edge plasma safety factor based on 0-D parameters[85]
q_{95}	Edge safety factor	Plasma safety factor at 95% flux surface
P_{aux}	Auxiliary power	Total external power used for plasma H&CD
P_{fusion}	Fusion power	Total power produced via fusion reactions in plasma core
P_{net}	Net power	Total net electric power produced by FPP
P_{SOL}	SOL power	Exhaust power across plasma boundary
R_0	Major radius	Radial distance from device centerline to plasma center
T_{i0}	Core ion temperature	Ion temperature at magnetic axis
β_N	Normalized beta	β normalized by factor I_P/aB_T
$\beta_{N,IW}$	Ideal-wall beta limit	Maximum β_N before MHD instability onset
β_P	Poloidal beta	Ratio of plasma pressure to poloidal magnetic field pressure
β_T	Toroidal beta	Ratio of plasma pressure to toroidal magnetic field pressure
δ	Triangularity	Ratio of plasma X-point radial distance from plasma center to minor radius
η_{aux}	H&CD efficiency	Conversion efficiency from plug power to injected power for H&CD systems
$\eta_{thermal}$	Thermal efficiency	Conversion efficiency from thermal cycle power to electrical power
$\eta_{reclaim}$	Reclaim efficiency	Conversion efficiency from reclaimed auxiliary power to thermal cycle
κ	Elongation	Ratio of plasma boundary height to boundary width at separatrix

(Continued)

TABLE A.I (Continued)

Symbol	Parameter Name	Definition
$v_e^\star$	Normalized collisionality	Neoclassical electron collisionality (volume-averaged params)[86]
$\rho^\star$	Relative gyroradius	Ratio of ion gyroradius (volume-averaged params) to plasma minor radius
ρ	Toroidal flux coordinate	Normalized radial flux coordinate based on enclosed toroidal flux
ψ_N	Poloidal flux coordinate	Normalized radial flux coordinate based on enclosed poloidal flux
ω_{ce0}	EC frequency	Calculated at magnetic axis
ω_{pe0}	Plasma electron frequency	Calculated at magnetic axis

Acknowledgments

Disclosure Statement

No potential conflict of interest was reported by the author(s).

ORCID

D. B. Weisberg http://orcid.org/0000-0003-4510-0884
J. McClenaghan http://orcid.org/0000-0003-4735-0991
J. Barr http://orcid.org/0000-0001-7768-5931
B. Grierson http://orcid.org/0000-0001-5918-6506
O. Meneghini http://orcid.org/0000-0001-5100-5483
C. C. Petty http://orcid.org/0000-0003-4534-9073
R. I. Pinsker http://orcid.org/0000-0003-2683-9480
W. M. Solomon http://orcid.org/0000-0002-0902-9876
D. Thomas http://orcid.org/0000-0002-1217-7773

References

1. T. CARTER et al., "Powering the Future: Fusion and Plasmas," Fusion Energy Science Advisory Committee (2020); https://usfusionandplasmas.org/wp-content/themes/FESAC/FESAC_Report_2020_Powering_the_Future.pdf.

2. S. BAALRUD et al., "A Community Plan for Fusion Energy and Discovery Plasma Sciences," 2019–2020 American Physical Society Division of Plasma Physics Community Planning Process (2020); https://sites.google.com/pppl.gov/dpp-cpp.

3. NATIONAL ACADEMIES OF SCIENCES, ENGINEERING, AND MEDICINE, "Bringing Fusion to the U.S. Grid," The National Academies Press (2021); https://doi.org/10.17226/25991.

4. M. KIKUCHI, "Prospects of a Stationary Tokamak Reactor," Plasma Phys. Control. Fusion, 35, B39 (1993); https://doi.org/10.1088/0741-3335/35/SB/003.

5. T. C. LUCE et al., "Development of Advanced Inductive Scenarios for ITER," Nucl. Fusion, 54, 013015 (2014); https://doi.org/10.1088/0029-5515/54/1/013015.

6. R. C. WOLF et al., "Stationary Advanced Scenarios with Internal Transport Barrier on ASDEX Upgrade," Plasma Phys. Control. Fusion, 41, B93 (1999); https://doi.org/10.1088/0741-3335/41/12B/306.

7. C. C. PETTY et al., "High-Beta, Steady-State Hybrid Scenario on DIII-D," Nucl. Fusion, 56, 016016 (2016); https://doi.org/10.1088/0029-5515/56/1/016016.

8. K. BESSEGHIR et al., "Achieving and Sustaining Advanced Scenarios in ITER Modelled by CRONOS and DINA-CH," Plasma Phys. Control. Fusion, 55, 125012 (2013); https://doi.org/10.1088/0741-3335/55/12/125012.

9. B. N. SORBUM et al., "ARC: A Compact, High-Field, Fusion Nuclear Science Facility and Demonstration Power Plant with Demountable Magnets," Fusion Eng. Des., 100, 378 (2015); https://doi.org/10.1016/j.fusengdes.2015.07.008.

10. C. E. KESSEL et al., "The ARIES Advanced and Conservative Tokamak Power Plant Study," Fusion Sci. Technol., 67, 1 (2015); https://doi.org/10.13182/FST14-794.

11. R. J. BUTTERY et al., "The Advanced Tokamak Path to a Compact Net Electric Fusion Pilot Plant," Nucl. Fusion, 61, 046028 (2020); https://doi.org/10.1088/1741-4326/abe4af.

12. L. MUZZI et al., "Cable-In-Conduit Conductors: Lessons from the Recent Past for Future Developments with Low and High Temperature Superconductors," Supercond. Sci. Technol., 28, 053001 (2015); https://doi.org/10.1088/0953-2048/28/5/053001.

13. N. MITCHELL et al., "Superconductors for Fusion: A Roadmap," Supercond. Sci. Technol., 34, 103001 (2021); https://doi.org/10.1088/1361-6668/ac0992.

⊗ANS

14. R. D. STAMBAUGH et al., "Fusion Nuclear Science Facility Candidates," *Fusion Sci. Technol.*, **59**, 279 (2011); https://doi.org/10.13182/FST59-279.

15. M. R. WADE and J. A. LEUER, "Cost Drivers for a Tokamak-Based Compact Pilot Plant," *Fusion Sci. Technol.*, **77**, 119 (2021); https://doi.org/10.1080/15361055.2020.1858670.

16. C. E. KESSEL et al., "Plasma Profile and Shape Optimization for the Advanced Tokamak Power Plant, ARIES-AT," *Fusion Eng. Des.*, **80**, 63 (2006); https://doi.org/10.1016/j.fusengdes.2005.06.350.

17. G. FEDERICI et al., "DEMO Design Activity in Europe: Progress and Updates," *Fusion Eng. Des.*, **136**, 729 (2018); https://doi.org/10.1016/j.fusengdes.2018.04.001.

18. T. EICH et al., "Scaling of the Tokamak Near the Scrape-Off Layer H-mode Power Width and Implications for ITER," *Nucl. Fusion*, **53**, 093031 (2013); https://doi.org/10.1088/0029-5515/53/9/093031.

19. M. L. REINKE et al., "Heat Flux Mitigation by Impurity Seeding in High-Field Tokamaks," *Nucl. Fusion*, **57**, 034004 (2017); https://doi.org/10.1088/1741-4326/aa5145.

20. D. KRAFT, "A Software Package for Sequential Quadratic Programming," Technical Report DFVLR-FB 88-28, DLR German Aerospace Center, Institute for Flight Mechanics, Koln, Germany (1988).

21. C. E. KESSEL et al., "Overview of the Fusion Nuclear Science Facility, a Credible Break-In Step on the Path to *Fusion* Energy," *Fusion Eng. Des.*, **135**, 236 (2018); https://doi.org/10.1016/j.fusengdes.2017.05.081.

22. C. C. PETTY et al., "Feasibility Study of a Compact Ignition Tokamak Based upon GyroBohm Scaling Physics," *Fusion Sci. Technol.*, **43**, 1 (2003); https://doi.org/10.13182/FST03-A245.

23. C. C. PETTY et al., "Scaling of Heat Transport with Beta in the DIII-D Tokamak," *Nucl. Fusion*, **38**, 1183 (1998); https://doi.org/10.1088/0029-5515/38/8/306.

24. ITER PHYSICS BASIS EXPERT GROUPS ON CONFINEMENT AND TRANSPORT et al., "Chapter 2: Plasma Confinement and Transport," *Nucl. Fusion*, **39**, 2175 (1999); https://doi.org/10.1088/0029-5515/39/12/302.

25. C. C. PETTY et al., "Beta Scaling of Transport on the DIII-D Tokamak: Is Transport Electrostatic or Electromagnetic?," *Phys. Plasmas*, **11**, 2514 (2004); https://doi.org/10.1063/1.1666263.

26. A. M. GAROFALO et al., "Compatibility of Internal Transport Barrier with Steady-State Operation in the High Bootstrap Fraction Regime on DIII-D," *Nucl. Fusion*, **55**, 123025 (2015); https://doi.org/10.1088/0029-5515/55/12/123025.

27. S. DING et al., "Confinement Improvement in the High Poloidal Beta Regime on DIII-D and Application to Steady-State H-Mode on EAST," *Phys. Plasmas*, **24**, 056114 (2017); https://doi.org/10.1063/1.4982058.

28. J. P. QIAN et al., "Advances in the High Bootstrap Fraction Regime on DII-D Towards the Q = 5 Mission of ITER Steady State," *Nucl. Fusion*, **57**, 056008 (2017); https://doi.org/10.1088/1741-4326/aa626a.

29. A. M. GAROFALO et al., "Joint DIII-D/EAST Research on the Development of a High Poloidal Beta Scenario for the Steady State Missions of ITER and CFETR," *Plasma Phys. Control. Fusion*, **60**, 014043 (2018); https://doi.org/10.1088/1361-6587/aa8c9d.

30. J. LUXON, "A Design Retrospective of the DIII-D Tokamak," *Nucl. Fusion*, **42**, 614 (2002); https://doi.org/10.1088/0029-5515/42/5/313.

31. H. MEYER et al., "Overview of Physics Studies on ASDEX Upgrade," *Nucl. Fusion*, **59**, 112014 (2019); https://doi.org/10.1088/1741-4326/ab18b8.

32. M. KWON et al., "Overview of KSTAR Initial Operation," *Nucl. Fusion*, **51**, 094006 (2011); https://doi.org/10.1088/0029-5515/51/9/094006.

33. S. W. YOON et al., "Characteristics of the First H-mode Discharges in KSTAR," *Nucl. Fusion*, **51**, 113009 (2011); https://doi.org/10.1088/0029-5515/51/11/113009.

34. S. WU et al., "An Overview of the EAST Project," *Fusion Eng. Des.*, **82**, 463 (2007); https://doi.org/10.1016/j.fusengdes.2007.03.012.

35. M. K. A. THUMM et al., "High-Power Gyrotrons for Electron Cyclotron Heating and Current Drive," *Nucl. Fusion*, **59**, 073001 (2019); https://doi.org/10.1088/1741-4326/ab2005.

36. O. MENEGHINI et al., "Neural-Network Accelerated Coupled Core-Pedestal Simulations with Self-Consistent Transport of Impurities and Compatible with ITER IMAS," *Nucl. Fusion*, **61**, 026006 (2021); https://doi.org/10.1088/1741-4326/abb918.

37. X. BONNIN et al., "Presentation of the New SOLPS-ITER Code Package for Tokamak Plasma Edge Modelling," *Plasma Fusion Res.*, **11**, 1403102 (2016); https://doi.org/10.1585/pfr.11.1403102.

38. D. A. HUMPHREYS et al., "Development of ITER-Relevant Plasma Control Solutions at DIII-D," *Nucl. Fusion*, **47**, 943 (2007); https://doi.org/10.1088/0029-5515/47/8/028.

39. M. WALKER and D. HUMPHREYS, "Valid Coordinate Systems for Linearized Plasma Shape Response Models in Tokamaks," *Fusion Sci. Technol.*, **50**, 473 (2006); https://doi.org/10.13182/FST06-A1271.

40. P. ROMANO et al., "OpenMC: A State-of-the-Art Monte Carlo Code for Research and Development," *Ann. Nucl. Energy*, **82**, 90 (2015); https://doi.org/10.1016/j.anucene.2014.07.048.

41. C. T. HOLCOMB et al., "Steady State Scenario Development with Elevated Minimum Safety Factor on DIII-D," *Nucl. Fusion*, **54**, 093009 (2014); https://doi.org/10.1088/0029-5515/54/9/093009.

42. P. B. SNYDER et al., "High Fusion Performance in Super H-mode Experiments on Alcator C-Mod and DIII-D," *Nucl. Fusion*, **59**, 086017 (2019); https://doi.org/10.1088/1741-4326/ab235b.

43. L. LAO et al., "MHD Equilibrium Reconstruction in the DIII-D Tokamak," *Fusion Sci. Technol.*, **48**, 968 (2005); https://doi.org/10.13182/FST48-968.

44. H. LUTJENS et al., "The CHEASE Code for Toroidal MHD Equilibria," *Comput. Phys. Commun.*, **97**, 219 (1996); https://doi.org/10.1016/0010-4655(96)00046-X.

45. P. B. SNYDER et al., "Development and Validation of a Predictive Model for the Pedestal Height," *Phys. Plasmas*, **16**, 056118 (2009); https://doi.org/10.1063/1.3122146.

46. E. BELLI and J. CANDY, "Full Linearized Fokker-Planck Collisions in Neoclassical Transport Simulations," *Plasma Phys. Control. Fusion*, **54**, *1*, 015015 (2011); https://doi.org/10.1088/0741-3335/54/1/015015.

47. H. ST. JOHN et al., "Transport Simulation of Negative Magnetic Shear Discharges," *Proc. 15th Int. Conf. on Plasma Physics and Control Nuclear Fusion Research*, Seville, Spain, Vol. 1 (1994)

48. J. CANDY et al., "Tokamak Profile Prediction Using Direct Gyrokinetic and Neoclassical Simulation," *Phys. Plasmas*, **16**, 060704 (2009); https://doi.org/10.1063/1.3167820.

49. A. GLASSER, "The Direct Criterion of Newcomb for the Ideal MHD Stability of an Axisymmetric Toroidal Plasma," *Phys. Plasmas*, **23**, 072505 (2016); https://doi.org/10.1063/1.4958328.

50. S. L. GRALNICK and F. H. TENNEY, "Analytic Solutions for Constant Tension Coil Shapes," Technical Report, Princeton Plasma Physics Laboratory (1976).

51. D. C. VAN DER LAAN et al., "Characterization of a High-Temperature Superconducting Conductor on Round Core Cables in Magnetic Fields up to 20 T," *Supercond. Sci. Technol.*, **26**, 045005 (2013); https://doi.org/10.1088/0953-2048/26/4/045005.

52. Y. ZHAI et al., "Conceptual Design of HTS Magnets for Fusion Nuclear Science Facility," *Fusion Eng. Des.*, **168**, 112611 (2021); https://doi.org/10.1016/j.fusengdes.2021.112611.

53. D. HUMPHREYS et al., "Experimental Vertical Stability Studies for ITER Performance and Design Guidance," *Nucl. Fusion*, **49**, 115003 (2009); https://doi.org/10.1088/0029-5515/49/11/115003.

54. D. BRUNNER et al., "The Dependence of Divertor Power Sharing on Magnetic Flux Balance in Near Double-Null Configurations on Alcator C-Mod," *Nucl. Fusion*, **58**, 076010 (2018); https://doi.org/10.1088/1741-4326/aac006.

55. R. SCHNEIDER et al., "Plasma Edge Physics with B2-Eirene," *Contrib. Plasma Phys.*, **46**, 3 (2006); https://doi.org/10.1002/ctpp.200610001.

56. D. REITER et al., "The EIRENE and B2-EIRENE Codes," *Fusion Sci. Technol.*, **47**, 172 (2017); https://doi.org/10.13182/FST47-172.

57. H. Y. GUO et al., "Small Angle Slot Divertor Concept for Long Pulse Advanced Tokamaks," *Nucl. Fusion*, **57**, 044001 (2017); https://doi.org/10.1088/1741-4326/aa5b46.

58. R. MAURIZIO et al., "Numerical Assessment of the New V-shape Small-Angle Slot Divertor on DIII-D," *Nucl. Fusion*, **61**, 116042 (2021); https://doi.org/10.1088/1741-4326/ac27c8.

59. A. L. MOSER et al., "Separating Divertor Closure Effects on Divertor Detachment and Pedestal Shape in DIII-D," *Phys. Plasmas*, **27**, 032506 (2020); https://doi.org/10.1063/1.5109027.

60. H. REIMERDES et al., "Initial TCV Operation with a Baffled Divertor," *Nucl. Fusion*, **61**, 024002 (2021); https://doi.org/10.1088/1741-4326/abd196.

61. R. PITTS et al., "Physics Basis for the First ITER Tungsten Divertor," *Nucl. Mat. Energy*, **20**, 100696 (2019); https://doi.org/10.1016/j.nme.2019.100696.

62. J. NEUHAUSER et al., "The Compatibility of High Confinement Times and Complete Divertor Detachment in ASDEX-Upgrade," *Plasma Phys. Control. Fusion*, **37**, A37 (1995); https://doi.org/10.1088/0741-3335/37/11A/003.

63. A. KALLENBACK et al., "Partial Detachment of High Power Discharges in ASDEX Upgrade," *Nucl. Fusion*, **55**, 053026 (2015); https://doi.org/10.1088/0029-5515/55/5/053026.

64. L. CASALI et al., "Improved Core-Edge Compatibility Using Impurity Seeding in the Small Angle Slot (SAS) Divertor at DIII-D," *Phys. Plasmas*, **27**, 062506 (2020); https://doi.org/10.1063/1.5144693.

65. J. SHIMWELL et al., "The Paramak: Automated Parametric Geometry Construction for Fusion Reactor Designs," *F1000Research*, **10**, 27 (2021); https://doi.org/10.12688/f1000research.28224.1.

66. P. WILSON et al., "Acceleration Techniques for the Direct Use of CAD-Based Geometry in Fusion Neutronics Analysis," *Fusion Eng. Des.*, **85**, 1759 (2010); https://doi.org/10.1016/j.fusengdes.2010.05.030.

67. T. BLACKER et al., "Cubit Mesh Generation Environment. Volume 1: Users Manual," Technical Report SAND-94-1100, Sandia National Laboratories (1994).

68. J. KIM et al., "Radiation Shielding Analysis for DII-d," *Proc. IEEE 13th Symp. on Fusion Engineering*, p. 869, Institute of Electrical and Electronics Engineers (1989).

69. J. W. HUGHES et al., "Access to Pedestal Pressure Relevant to Burning Plasmas on the High Magnetic Field Tokamak Alcator C-Mod," *Nucl. Fusion*, **58**, 112003 (2018); https://doi.org/10.1088/1741-4326/aabc8a.

70. R. VONDRACEK et al., "Preliminary Design of the COMPASS Upgrade Tokamak," *Fusion Eng. Des.*, **169**,

112490 (2021); https://doi.org/10.1016/j.fusengdes.2021. 112490.

71. R. AMBROSINO et al., "DTT—Divertor Tokamak Test Facility: A Testbed for DEMO," *Fusion Eng. Des.*, **167**, 112330 (2021); https://doi.org/10.1016/j.fusengdes.2021. 112330.

72. A. J. CREELY et al., "Overview of the SPARC Tokamak," *J. Plasma Phys.*, **86**, 865860502 (2020); https://doi.org/10. 1017/S0022377820001257.

73. T. CASPER et al., "Development of the ITER Baseline Inductive Scenario," *Nucl. Fusion*, **54**, 013005 (2014); https://doi.org/10.1088/0029-5515/54/1/013005.

74. E. A. LAZARUS et al., "Higher Fusion Power Gain with Profile Control in DIII-D Tokamak Plasmas," *Nucl. Fusion*, **37**, 7 (1997); https://doi.org/10.1088/0029-5515/ 37/1/I11.

75. T. C. LUCE et al., "Long Pulse High Performance Discharges in the DIII-D Tokamak," *Nucl. Fusion*, **41**, 1585 (2001); https://doi.org/10.1088/0029-5515/41/11/308.

76. V. S. CHAN et al., "DIII-D Advanced Tokamak Research Overview," *Nucl. Fusion*, **40**, 1137 (2000); https://doi.org/ 10.1088/0029-5515/40/6/311.

77. S. ISHIDA et al., "JT-60U High Performance Regimes," *Nucl. Fusion*, **39**, 1211 (1999); https://doi.org/10.1088/ 0029-5515/39/9Y/301.

78. M. KEILHACKER et al., "High Fusion Performance from Deuterium-Tritium Plasmas in JET," *Nucl. Fusion*, **39**, 209 (1999); https://doi.org/10.1088/0029-5515/39/2/306.

79. S. SAARELMA et al., "Integrated Modelling of H-mode Pedestal and Confinement in JET-ILW," *Plasma Phys. Control. Fusion*, **60**, 014042 (2017); https://doi.org/10. 1088/1361-6587/aa8d45.

80. R. J. HAWRYLUK et al., "Fusion Plasma Experiments on TFTR: A 20 Year Retrospective," *Phys. Plasmas*, **5**, 1577 (1998); https://doi.org/10.1063/1.872825.

81. T. KLINGER et al., "Overview of First Wendelstein 7-X High-Performance Operation," *Nucl. Fusion*, **59**, 112004 (2019); https://doi.org/10.1088/1741-4326/ab03a7.

82. M. SHIMADA et al., "Chapter 1: Overview and Summary," *Nucl. Fusion*, **47**, S1 (2007); https://doi.org/ 10.1088/0029-5515/47/6/S01.

83. S. EJIMA et al., "Volt-Second Analysis and Consumption in Doublet III Plasmas," *Nucl. Fusion*, **22**, 1313 (1982); https://doi.org/10.1088/0029-5515/22/10/006.

84. R. D. STAMBAUGH et al., "Relation of Vertical Stability and Aspect Ratio in Tokamaks," *Nucl. Fusion*, **32**, 1642 (1992); https://doi.org/10.1088/0029-5515/32/9/I12.

85. N. A. UCKAN et al., "ITER Physics Design Guidelines: 1989," Technical Report 10, International Atomic Energy Agency (1990).

86. O. SAUTER et al., "Neoclassical Conductivity and Bootstrap Current Formulas for General Axisymmetric Equilibria and Arbitrary Collisionality Regime," *Phys. Plasmas*, **6**, 2834 (1999); https://doi.org/10.1063/1. 873240.